Design of a metal additive manufactured aircraft seat leg using topology optimization and part decomposition

Hansu Kim, Luke Crispo, Anuj Patel and Nicholas Galley

Department of Mechanical and Materials Engineering, Queen's University, Kingston, Canada

Si Mo Yeon and Yong Son

Advanced Joining and Additive Manufacturing R&D Department, Korea Institute of Industrial Technology, Siheung-si, Republic of Korea, and

Il Yong Kim

Department of Mechanical and Materials Engineering, Queen's University, Kingston, Canada

Abstract

Purpose – Lightweight design of aircraft seats can significantly improve fuel efficiency and reduce greenhouse gas emissions. Metal additive manufacturing can produce lightweight topology-optimized designs with improved performance, but limited build volume restricts the printing of large components. The purpose of this paper is to design a lightweight aircraft seat leg structure using topology optimization and metal additive manufacturing with build volume restrictions, while satisfying structural airworthiness certification requirements.

Design/methodology/approach – Topology optimization was used to determine a lightweight conceptual design for the seat leg structure. The conceptual design was decomposed to meet the machine build volume, a detailed CAD assembly was designed, and print orientation was selected for each component. Static and dynamic verification was performed, the design was updated to meet the structural requirements, and a prototype was manufactured.

Findings – The final topology-optimized seat leg structure was decomposed into three parts, yielding a 57% reduction in the number of parts compared to a reference design. In addition, the design achieved an 8.5% mass reduction while satisfying structural requirements for airworthiness certification.

Originality/value – This study is the first paper to design an aircraft seat leg structure manufactured with metal additive manufacturing using a rigorous topology optimization approach. The resultant design reduces mass and part count compared to a reference design and is verified with respect to real-world aircraft certification requirements.

Keywords Aircraft seat leg, Structural airworthiness certification, Metal additive manufacturing, Topology optimization, Build volume, Part decomposition, Build orientation

Paper Type Research paper

1 Introduction

The aerospace industry is constantly exploring lightweighting opportunities, with a particular focus on aircraft seat design (Gulavani *et al.,* 2014; Hughes *et al.,* 2014; Trivers *et al.,* 2020; Noronha *et al.,* 2021; Roper *et al.,* 2021; Tzanakis *et al.,* 2023). As mass savings are compounded across every seat in the aircraft, a ~55% reduction in seat frame mass could lead to fuel savings of up to USD 200 million and a reduction of up to 140,000 tons of carbon in the atmosphere over the 20-year life of a fleet of 100 Airbus A380s (Autodesk, 2017). This is one reason why the global aircraft seat market size is projected to grow from USD 6.94 billion in 2022 to USD 9.25 billion in 2029 (Fortune Business Insights, 2022). However, aircraft seat design is a complex engineering challenge because the seat is the primary load path between the passenger and the aircraft and therefore must meet Federal Aviation Administration regulations to receive structural airworthiness certification. This involves a series of stringent tests with static and dynamic loading to ensure that: the aircraft seat remains connected to the seat track, the primary load paths remain intact, and occupants will be protected during an emergency landing scenario (CFR, 2023; SAE, 2020). Many aircraft seats may be overdesigned in efforts to pass structural airworthiness certification, which can lead to increased aircraft weight and decreased fuel efficiency.

Metal additive manufacturing (MAM) can help in lightweighting aircraft seats because it can produce complex and organic metallic structures with improved performance (Blakey-Milner *et al.,* 2021). To leverage the capabilities of MAM, components must be designed from conception specifically for MAM. Topology optimization

(TO) enables this goal by determining the optimal material distribution within a design space that maximizes performance subject to design requirements (Bendsøe and Kikuchi, 1988; Bendsøe and Sigmund, 2003). There has been increased attention in the integration of TO methods into MAM design workflow, especially within the aerospace, automotive, and medical industries (Ibhadode, 2023). For the aerospace industry, brackets (Seabra *et al.,* 2016; López-Castro *et al.,* 2017; Shi *et al.,* 2020; Willner *et al.,* 2020; Prathyusha and Babu, 2022), a cargo door component (Wiberg *et al.,* 2021), a door lever (Berrocal et al., 2019), a housing component (Berrocal *et al.,* 2019), and a connector support (Berrocal *et al.,* 2019) were topologically optimized and produced via MAM machines.

Aircraft seat legs have been designed in literature using finite element (FE) analysis approaches (Gulavani *et al.,* 2014; Hughes *et al.,* 2014; Tzanakis *et al.,* 2023). Seat leg structural design has also been conducted with topology optimization using a pseudo-force technique (Noronha *et al.,* 2021) and based on structural airworthiness certification requirements (Trivers *et al.,* 2020; Roper *et al.,* 2021). Despite the increased design freedom possible with MAM and the potential for significant mass reductions from a system level viewpoint, no studies have conducted rigorous TO-based design for an aircraft seat leg with MAM.

The limited build volume of MAM machines restricts the printing of large components, such as an aircraft seat leg. Large components must instead be decomposed into several parts to achieve printability, in a process known as part decomposition (PD) (Chan and Tan, 2005; Oh *et al.,* 2018; Zhou *et al.,* 2019; Morin and Kim; 2022). In addition to these build volume constraints, the design of MAM components should also consider support structure requirements, which are needed to print overhanging surfaces and to prevent thermal distortion (Oh *et al.,* 2021). Support structures increase build time and cost but can be reduced through geometry changes and by optimizing build orientation (Fritz and Kim, 2020; Olsen and Kim, 2020). To successfully design a lightweight aircraft seat leg using MAM, the PD process (considering build volume, build orientation, and support structure) must be integrated into the TO workflow.

The objective of this study is to use a rigorous TO-based approach to design a lightweight MAM aircraft seat leg structure that meets real-world aircraft certification requirements. To achieve this goal, a new TO workflow is presented for the design of large additive manufacturing components, incorporating decomposition into parts based on build volume and selection of build orientation based on support volume and thermal considerations. A

conceptual seat leg structure is designed with TO and decomposed using partitioning blocks to meet MAM build volume limits. A detailed assembly CAD model is developed, and the build orientation of each part is selected considering support material, cross-sectional area, and tooling accessibility. The design is updated based on static and dynamic verifications to satisfy structural airworthiness certification requirements. Finally, a full scale seat leg prototype is fabricated via the DMP flex 350 to demonstrate that the proposed design is manufacturable with MAM. The outcome of the design process presented in this work is a novel seat leg assembly design for MAM that reduces weight and part count relative to a reference design in literature (Tzanakis *et al.,* 2023).

The remainder of the paper is organized to meet the research objectives. This begins with a thorough review of the structural requirements of aircraft seats in Section 2. This is followed by the proposed design methodology: 1) Conceptual Design Phase, 2) Detailed Design Phase, and 3) Verification Phase in Section 3. Then, the proposed design methodology is applied to the aircraft seat leg and details are explained with results of each phase in Sections 4, 5, and 6. Lastly, Section 7 provides the conclusions of this study.

2 Structural requirements

This section outlines the structural requirements for static and dynamic verification of a Transport Airplane Category type A-T seat derived from the Emergency Landing Condition in 14 CFR 25.561 and 25.562 (CFR, 2023). These certification requirements are outlined in further detail in SAE Aerospace Standard AS8049 (SAE, 2020).

2.1 Static certification requirements

Type A-T aircraft seats must withstand ultimate load factors with the load directions shown in Table 1. Ultimate loads were calculated using these factors and an occupant weight of 77 kg, which is the weight of a 50th percentile male Anthropomorphic Test Device (ATD) (SAE, 2020). The ultimate loads were applied to the ATD body blocks in Figure 1 at specific load application points based on the seat reference point (SRP) shown in Table 2. Readers are referred to SAE Aerospace Recommended Practice ARP5526 (SAE, 2018) for a detailed explanation of the SRP.

In addition to the ultimate load cases, three impact load cases and four abuse load cases were also considered for the static certification requirements as shown in Figure 2. The abuse load cases LC 3.1–3.3 were derived from headrest loads (SAE, 2020) and LC 3.4 was added as a

Figure 1 Ultimate load cases: (a) LC 1.1 Ultimate Load, Forward, (b) LC 1.2 Ultimate Load, Side (Left), (c) LC 1.3 Ultimate Load, Side (Right), (d) LC 1.4 Ultimate Load, Upward, (e) LC 1.5 Ultimate Load, Downward, (f) LC 1.6 Ultimate Load, Aftward
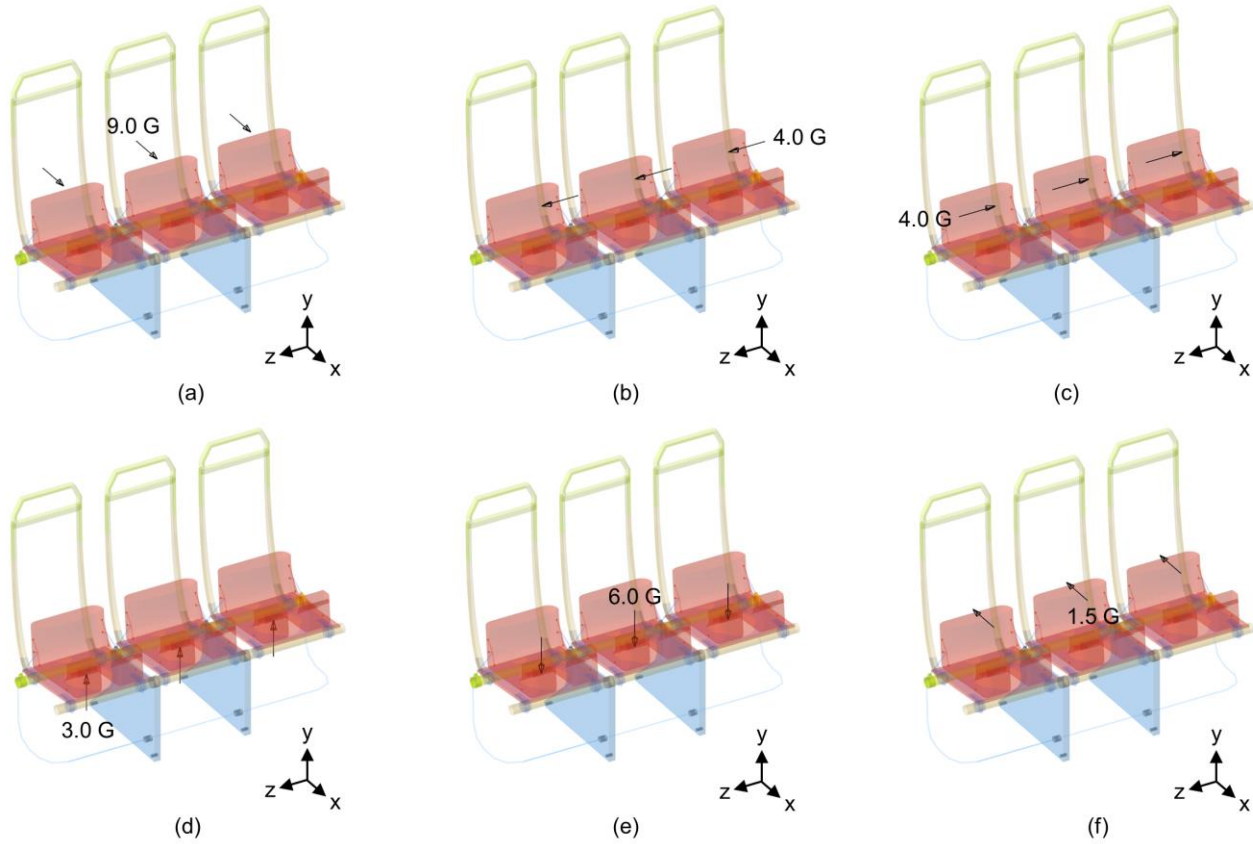

(a) (b) (c)

(d) (e) (f)

Table 1 Ultimate load factors for type A-T seats and load directions (SAE, 2020)

Load Direction	Load Factor (G-force)
Forward	9.0
Sideward	4.0
Upward	3.0
Downward	6.0
Aftward	1.5

Table 2 Static load application points of forward and rearward facing seats (SAE, 2020)

Load Direction	Load Application Point
Forward	270 mm up from the SRP
Sideward	270 mm up from the SRP and 215 mm forward of the SRP
Upward	215 mm forward of the SRP
Downward	Evenly over seat bottom
Aftward	270 mm up from the SRP

new twist load case. These loads were applied to the corner and center of the headrest. The impact load cases mimic the dynamic load conditions described in Section 2.2 and were applied to the load application points shown in Table 2. The dynamic tests were included as static loads for topology optimization, because TO sensitivities cannot be calculated for non-linear dynamic analysis without advanced methods (Jang *et al.,* 2012). While the linear static analysis will not accurately model the dynamic behavior of the structure, the dynamic loads will influence the TO solution to allocate material to stiffen the structure in the dynamic loading acceleration directions.

To pass the static tests, the seat structure must support the ultimate loads without failure for at least 3 seconds (SAE, 2020). This study used the minimum margin of safety (MoS) (Niu, 2001) as a failure criterion. For the seat leg structure, the MoS was calculated based on von Mises stress and buckling load factor as follows:

$$MoS_{von} \ [\%] = \left(\frac{\sigma_{ultimate}}{\sigma_{VM}^{max}} - 1 \right) \times 100 \qquad (1)$$

$$MoS_{buckling} \ [\%] = \left(\frac{F_{buckling}}{F_{applied}} - 1 \right) \times 100 \qquad (2)$$

Figure 2 Impact and abuse load cases: (a) LC 2.1 Impact Load, Forward (Left, 10 degree), (b) LC 2.2 Impact Load, Forward (Right, 10 degree), (c) LC 2.3 Impact Load, Downward (30 degree), (d) LC 3.1 Abuse Load, Corner Aftward, (e) LC 3.2 Abuse Load, Corner Forward, (f) LC 3.3 Abuse Load, Center, (g) LC 3.4 Abuse Load, Twist
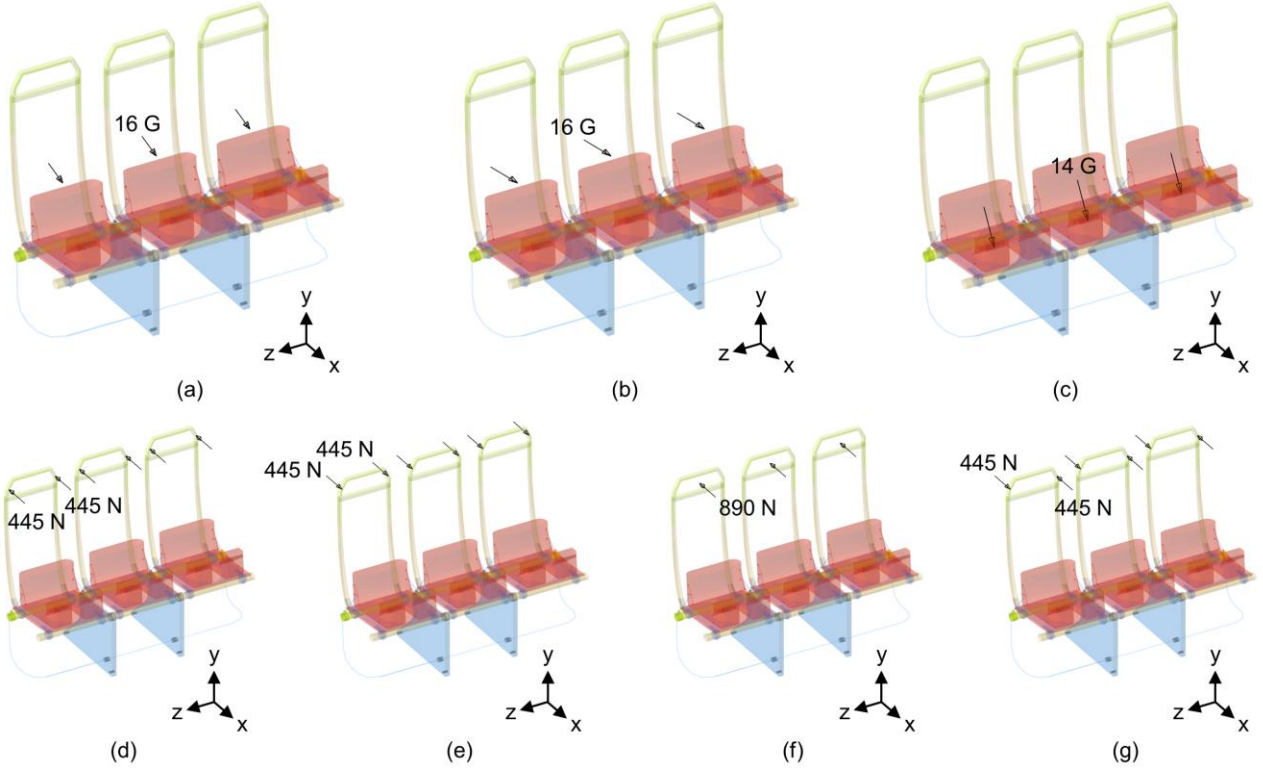
where $F_{applied}$ is the applied load, $F_{buckling}$ is the buckling load, $\sigma_{ultimate}$ is the ultimate tensile strength and σ_{VM}^{max} is the maximum von Mises stress. For the bolted joint regions, the MoS was calculated based on axial and shear forces, and bearing stresses as follows:

$$MoS_{axial} \ [\%] = \left(\frac{F_{axial}^{ultimate}}{F_{axial}^{max} \times FF} - 1 \right) \times 100 \qquad (3)$$

$$MoS_{shear} \ [\%] = \left(\frac{F_{shear}^{ultimate}}{F_{shear}^{max} \times FF} - 1 \right) \times 100 \qquad (4)$$

$$MoS_{bearing} \ [\%] = \left(\frac{\sigma_{bearing}^{ultimate}}{\sigma_{bearing}^{max} \times FF} - 1 \right) \times 100 \qquad (5)$$

where F_{axial}^{max} is the maximum axial force, $F_{axial}^{ultimate}$ is the ultimate axial force, F_{shear}^{max} is the maximum shear force, $F_{shear}^{ultimate}$ is an ultimate shear force, FF is a fitting factor of 1.15 according to 14 CFR 25.625, $\sigma_{bearing}^{max}$ is the maximum bearing stress, and $\sigma_{bearing}^{ultimate}$ is an ultimate bearing stress. The seat leg structure will be considered acceptable if the minimum values of the MoS for all 13 static load cases are above zero. If these criteria are met, the seat leg structure will be safe from material fracture,

geometric buckling, bolt fracture, and material fracture around bolt for the static loads.

2.2 Dynamic certification requirements

Transport category aircraft seats must successfully complete two dynamic tests as shown in Table 3. Dynamic test 1 has a combined downward and forward impact load, whereas dynamic test 2 has a predominantly forward impact load with a slight yaw angle. These tests evaluate the structural adequacy of the seat and permanent deformation of the structure under these two impact scenarios.

The dynamic tests are performed by applying a triangular deceleration pulse to the seat fixture (see Table 3). The deceleration pulse can be simulated by initializing the seat with the minimum velocity and decelerating it accordingly. For dynamic test 2, the seat is required to be pitched 10 degrees and rolled 10 degrees relative to the undeformed floor structure.

To pass the dynamic tests, the seat structure must remain attached at all seat track connection points and the primary load path must remain intact as described in SAE Aerospace Standard AS8049 (SAE, 2020). Because the tests represent crash loading conditions, some damage to the seat structure is allowed if the primary load path continues to exist between the occupant and the seat

Table 3 Dynamic tests for type A-T seats and images from SAE Aerospace Standard AS8049 (SAE, 2020)
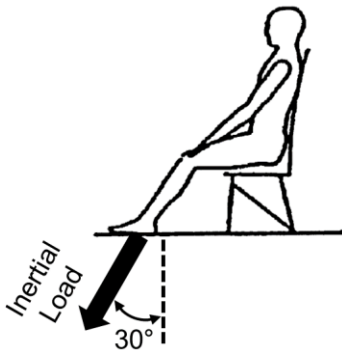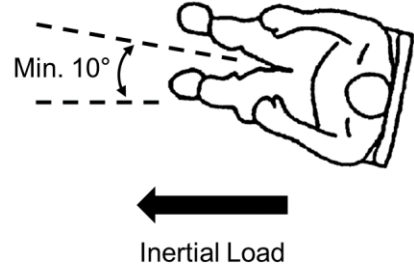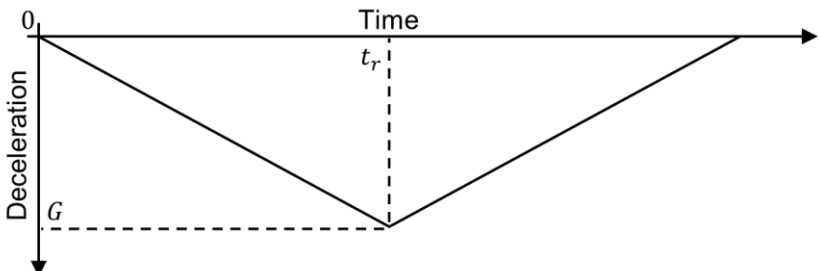
	Dynamic Test 1	Dynamic Test 2
Illustration (forward facing seat)		Yaw right or left Min. 10° Inertial Load
Minimum Velocity	10.67 m/s	13.41 m/s
Maximum Rise Time (t_r)	0.08 seconds	0.09 seconds
Minimum Inertial Load (G)	14 G	16 G
Floor Deformation (roll)	0 degree	Minimum 10 degree
Floor Deformation (pitch)	0 degree	Minimum 10 degree
Deceleration Pulse		

Figure 3 Overall geometry of aircraft seat structure
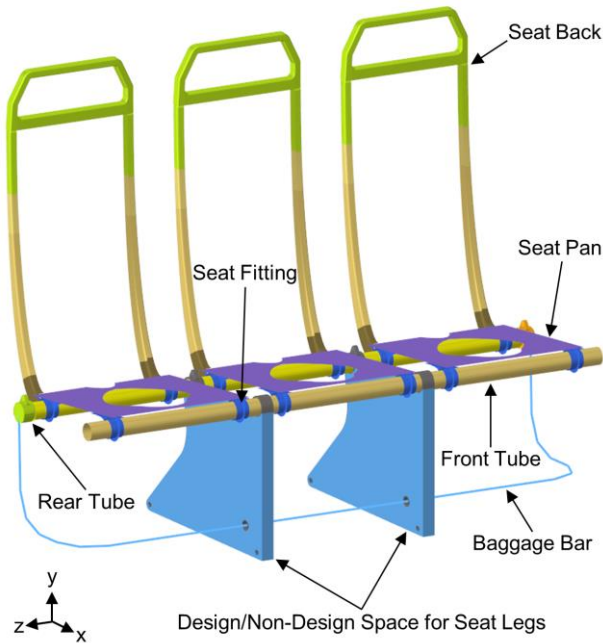
continues to exist between the occupant and the seat attachments. This study used the minimum MoS as a failure criterion based on plastic strain as follows:

$$MoS_{plastic}\ [\%] = \left(\frac{\varepsilon_{plastic}^{ultimate}}{\varepsilon_{plastic}^{max}} - 1 \right) \times 100 \qquad (6)$$

where $\varepsilon_{plastic}^{max}$ is the maximum plastic strain and $\varepsilon_{plastic}^{ultimate}$ is an ultimate plastic strain. The seat leg structure will be considered acceptable if the minimum values of the MoS are above zero or the primary load paths remain intact. However, the full fracture of any seat leg member is not allowed.

3   Design methodology

This section outlines the design methodology and rationale for the aircraft seat leg design space shown in Figure 3. The dimensions of the overall aircraft seat structure including seat back and seat pan are approximately $640 \times 1260 \times 1560\ \text{mm}$, and the material descriptions for each component are summarized

Figure 4 Flowchart of the entire design methodology
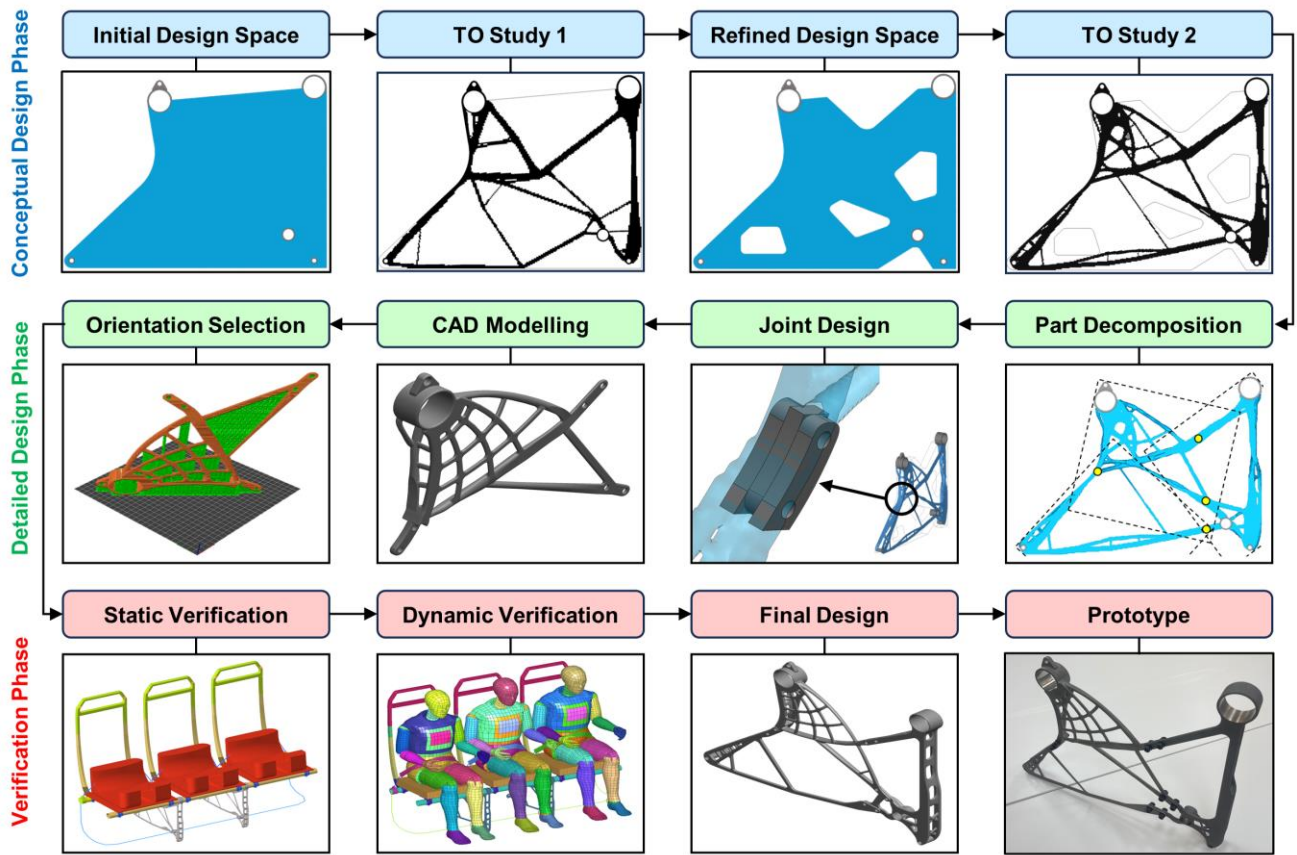
in Table A1 of Appendix 1. The flowchart of the entire design process is described in Figure 4. In the Conceptual Design Phase, TO was used to identify the primary load paths from the static load cases. The TO problem statement was defined to minimize compliance subjected to a mass fraction constraint. While this problem statement does not reflect the true structural requirements, it is highly effective for exploring conceptual designs to determine primary load paths. Two TO studies were performed to determine the conceptual design. In the first TO study, the TO problem was solved with varying mass fraction constraints based on the mass of a reference seat leg structure in literature (Tzanakis *et al.,* 2023). Next, the design space was refined by decreasing the element size to obtain more detailed features. In addition, the design space was reduced by removing the unneeded regions to improve computational time. In the second TO study, the TO problem was solved using the refined design space with varying mass fraction constraints and filter radii. Lastly, a TO solution was selected for the conceptual design based on compliance, joining regions, and design complexity.

In the first step of the Detailed Design Phase, PD was performed for the conceptual design. MAM can produce complex and organic metallic structures, but the printable size is limited by the MAM build volume. PD was required because the dimensions of the conceptual design were larger than the MAM build volume. Three partitioning blocks defined from the MAM build volume were used to decompose the conceptual design, with a primary design goal to minimize the number of parts and joining regions. Secondly, joint design was conducted to connect the decomposed parts. Among the several joining options, bolted joints were selected for their simplicity, lower risk during joining, ease of disassembly, ease of maintenance, and reliable performance, especially for aerospace applications. The dimensions of the bolted joints were determined based on aerospace recommendations (Niu, 2001). Thirdly, the conceptual design of the raw TO result was interpreted into a detailed CAD model considering the primary load paths and bolted joints. Lastly, build orientation was selected for each component based on support structure requirements and thermal distortion. For support structure requirements, volume of support material and tooling accessibility were evaluated using slicer software, while cross-sectional area was used as a metric for thermal distortion.

In the Verification Phase, static and dynamic load cases were used to verify the detailed seat leg structural design. The Johnson-Cook material model was used for

dynamic verification. The boundary conditions were defined from the SAE Aerospace Recommended Practices and Aerospace Standard documents (SAE, 2015; SAE 2018; SAE 2020). Changes were made to the detailed design to satisfy the structural requirements, because the Conceptual and Detailed Design Phases did not consider the nonlinear behavior modelled in the crashworthiness analysis. Lastly, a prototype of the seat leg structure was produced via the DMP Flex 350 MAM machine.

4   Conceptual design phase

In this section, TO studies were performed to determine a conceptual design from the static load cases.

4.1   Topology optimization problem statement

The mathematical problem statement for the TO was formulated as follows:

$$\underset{\underset{\sim}{x}}{\text{minimize}}\quad C_{total}\left(\underset{\sim}{x}\right)=\sum_{i=1}^{N}C_{i}\left(\underset{\sim}{x}\right)$$

$$\text{subject to}\quad \underset{\sim}{K}\left(\underset{\sim}{x}\right)\underset{\sim}{u}_{i}=\underset{\sim}{f}_{i},\quad i=1,..,N$$

$$g\left(\underset{\sim}{x}\right)=\frac{\sum_{e}x_{e}\rho V_{e}}{\sum_{e}\rho V_{e}}\leq \bar{W} \tag{7}$$

$$\forall \text{ element } e, x_{e}\in\left(0,1\right]$$

where C_i is the global compliance of the i-th load case, C_{total} is the total global compliance summed over the N load cases, $\underset{\sim}{f}_i$ is the external force vector of the i-th load case, $\underset{\sim}{K}$ is the global stiffness matrix, ρ is the physical density of the material, $\underset{\sim}{u}_i$ is the nodal displacement vector of the i-th load case, V_e is the element volume, $\bar{W}$ is the defined mass fraction, and x_e is the elemental density design variable value. Sensitivity filtering was used to avoid a numerical phenomenon known as checkerboarding (Sigmund, 2007).

A compliance-based problem statement was selected because it is well-behaved in TO and easily generates stiff designs for the specified set of applied loads and mass fraction constraint. Stress-constrained TO could be implemented to account for the static failure certification requirements (Holmberg *et al.*, 2013), but would add additional complexity and potential convergence issues, without addressing the dynamic loading requirements that are the limiting design criteria. Instead, the compliance problem statement was used to determine the best load paths for stiffness, and the stress and failure constraints were accounted for during the verification stage.

Figure 5 Design and non-design space of seat leg
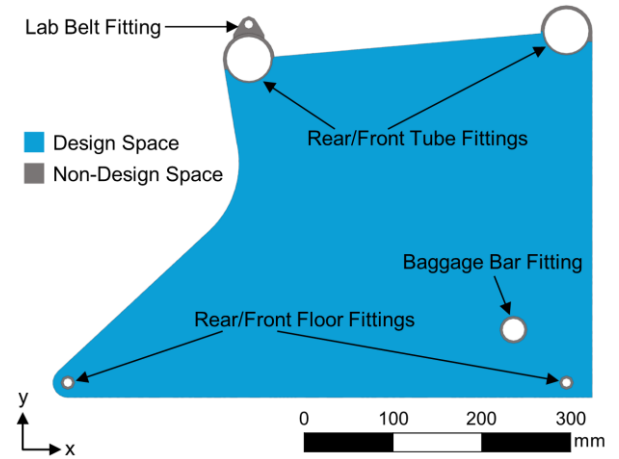
The design and non-design space of seat leg was defined as shown in Figure 5 based on aircraft seat designs in literature (Guida *et al.*, 2018; Roper *et al.*, 2021) and US Patents (Kismarton and Fullerton, 2013; Stachel et al., 2020). The material used for the design and non-design space was titanium, with generic material properties as follows: ρ is 4.50 g/cm³; Poisson's ratio is 0.32; and Young's modulus is 110 GPa. Lastly, the boundary conditions for TO are the same as described in Section 6.1.

4.2   Topology optimization study 1

The goal of the first TO study was to identify the primary load paths of the structure. To achieve this goal, TO was performed with varying mass fraction constraints. The reference mass fraction was calculated using the mass of a seat leg structure from literature (Tzanakis *et al.*, 2023) as follows:

$$\begin{aligned}\bar{W}_{ref}&=\frac{W_{ref}-W_{NDS}}{W_{DS}}\\&=\frac{2.305\text{ kg}-0.259\text{ kg}}{28.940\text{ kg}}=0.071\end{aligned} \tag{8}$$

where W_{DS} is the mass of design space, W_{NDS} is the mass of non-design space, W_{ref} is the reference mass of seat leg structure, and $\bar{W}_{ref}$ is the reference mass fraction. Based on $\bar{W}_{ref}$, TO was performed with a range of mass fractions (0.05, 0.06, 0.07, and 0.08) to view the influence of mass fraction limit on the resultant designs. The design and non-design space shown in Figure 5 was meshed using approximately 260,000 solid elements with an average element size of 3 mm. A filter radius of 9 mm (3× the average element size) was used for TO.

The TO problem was solved with an in-house topology optimization software that uses Altair OptiStruct for FE analysis. The results of TO Study 1 are shown in

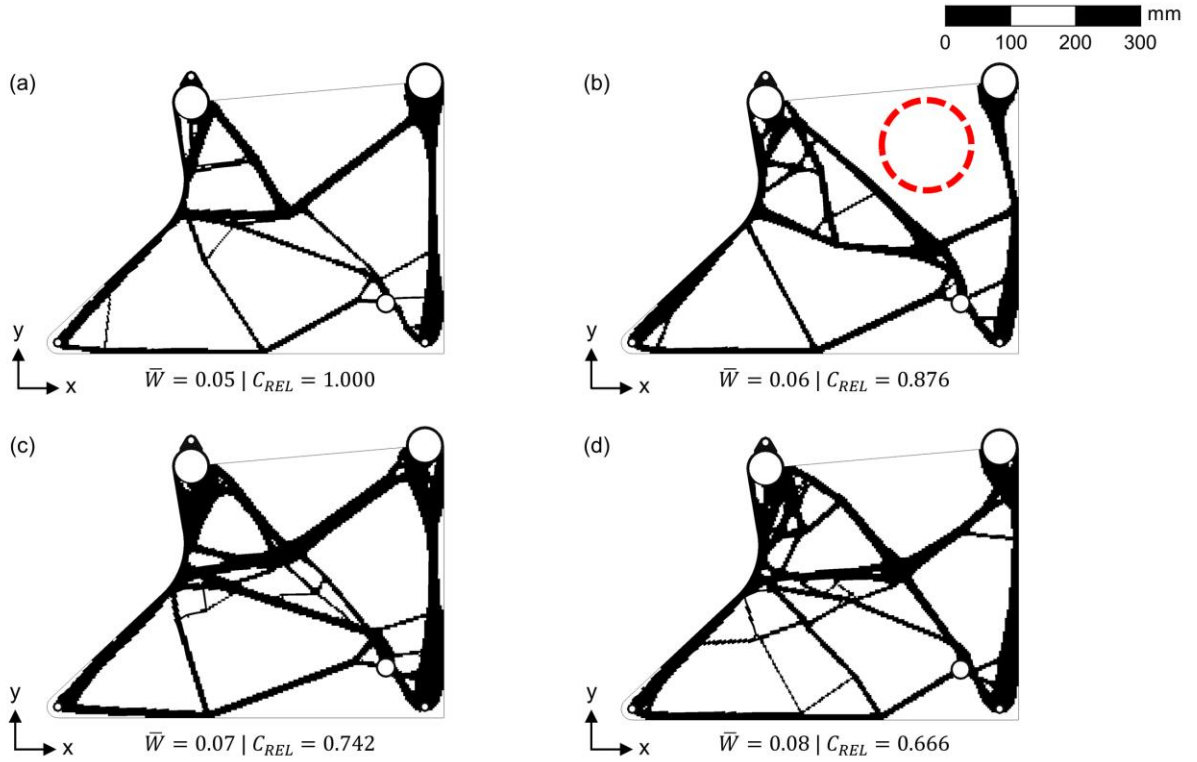**Figure 6** Thresholded element densities and relative compliance results from TO study 1

(a)
$\bar{W} = 0.05 \mid C_{REL} = 1.000$

(b)
$\bar{W} = 0.06 \mid C_{REL} = 0.876$

(c)
$\bar{W} = 0.07 \mid C_{REL} = 0.742$

(d)
$\bar{W} = 0.08 \mid C_{REL} = 0.666$

Figure 7 Overlap of TO results and definition of common void regions for removal

Figure 8 Refined design space of seat leg with a closeup of FE mesh in the boxed region
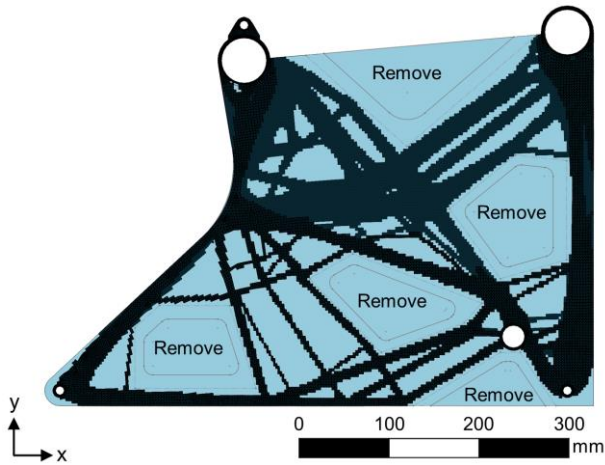
Figure 6, displaying only elements with a density greater than 0.5. The relative compliance was calculated by normalizing results relative to the mass fraction constraint with the highest compliance. Quantitatively, the results behave as expected, with relative compliance decreasing as mass fraction decreases.

Similar structural features were obtained for each of the mass fraction limits. However, in the 0.06 mass fraction case, a major structural member was omitted as shown in the red dotted circle. This result was classified as a local minimum when comparing to other mass fraction results. As the mass fraction increased, designs exhibited thicker primary structural members and an increase in thinner complex features.

4.3 Design space refinement

Before proceeding to the second TO study, the design space mesh was refined to obtain more detailed features. The minimum possible member size in TO is dictated by the sensitivity filtering radius, which has a minimum value of 1.5× the element size of the design space. By increasing the density of the design space mesh, smaller

Figure 9 Thresholded element densities and relative compliance results from TO study 2
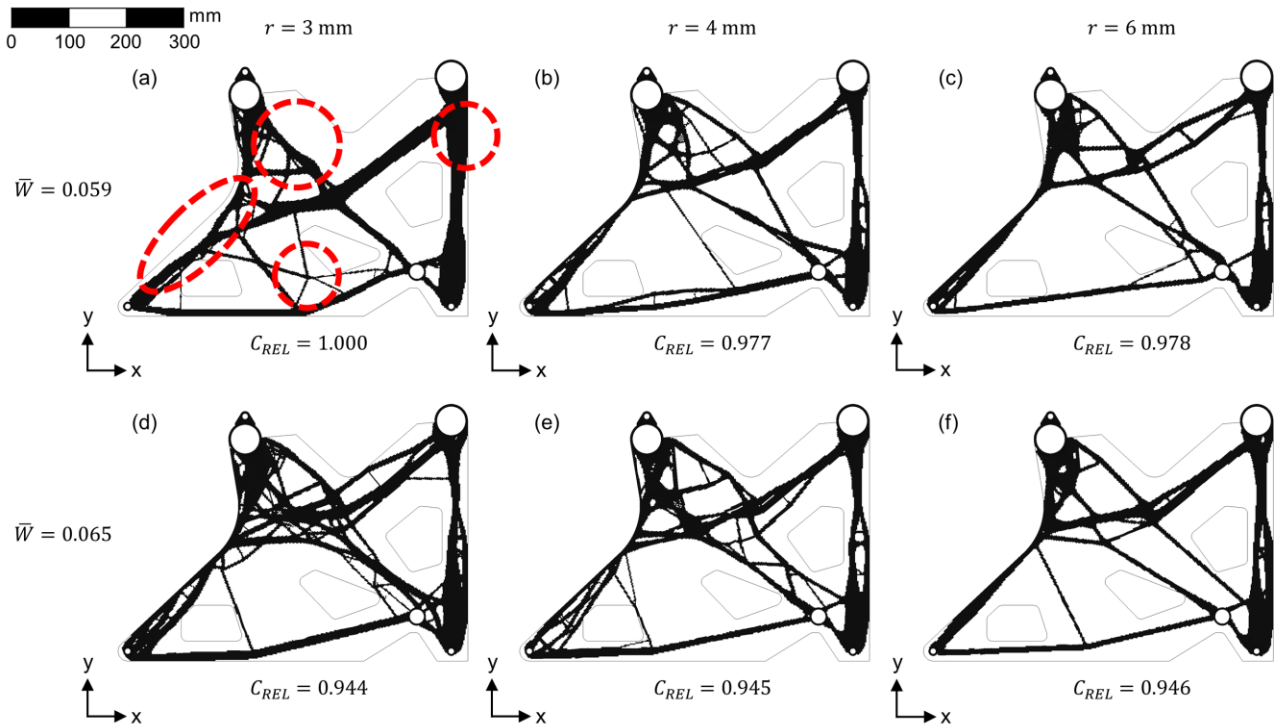
features can be formed due to the increased design variable resolution and a reduction in filter radius. However, the increase in mesh density is linked to a quadratic increase in computational time as the size of the global stiffness matrix increases. To reduce computational time, common void regions in the design space were removed by overlapping the results of the 0.05, 0.07, and 0.08 mass fractions as shown in Figure 7. Standard TO checkerboard filtering techniques can cause element density to "stick" to the outer edges of the design space (Clausen and Andreassen, 2017), so the cutouts were offset from the nearest members to avoid any influence on the TO study 2 results. The cutouts reduced the design space volume by approximately 20%, resulting in a meaningful reduction in computational time.

The refined design space of the seat leg is shown in Figure 8, with a reduction in average element size from 3 mm to 2 mm. With this element size, the design and non-design space of the seat leg was meshed using approximately 550,000 solid elements.

4.4 Topology optimization study 2
The goal of the second TO study was to produce more detailed features using the refined design space. More detailed features can result in improved performance due to the increased design freedom and can be easily manufactured with the MAM printing process. The reference mass fraction was re-calculated to be 0.059 using Equation (8), based on the 0.05 mass fraction and

the mass of the refined design space. In addition, TO was run with a 0.065 mass fraction constraint. To generate more detailed features, TO was performed with reduced filter radii, r, of 3 mm, 4 mm, and 6 mm (compared to the 9 mm filter radius used for TO study 1).

The results of TO Study 2 are shown in Figure 9, displaying only elements with a density greater than 0.5. The optimization in Figure 9 (a) produced features shown in the red dotted circles that were different from all other designs. As this result also had a larger compliance compared to equivalent mass fractions, it was classified as a poor local minimum and was eliminated as a potential design candidate. Other than this case, the results show similar main load paths and relative compliance increases with increasing filter radius as expected. This is because larger filter radii restrict the design freedom by forcing the optimizer to use larger member sizes.

As a whole, the 0.065 mass fraction designs in Figure 9 (d) – (f) resulted in a poor trade-off compared to the 0.059 mass fractions because they were 8% heavier, with only a 3% decrease in compliance. The heavier designs also had many thin and complex features compared to the primary structural members, which would significantly increase joining complexity and part decomposition. These designs were therefore also eliminated as potential candidates for the final conceptual design.

The results in Figure 9 (b) and (c) had nearly identical performance and Figure 9 (b) was therefore selected as the

final conceptual design (shown in detail in Figure 10) because of its smaller features which are better suited for the MAM process. The selected concept was used as a starting point and inspiration for the detailed design, and therefore the choice between these two designs was not expected to overly influence the performance of the final design.

5 Detailed design phase

In this section, a fully defined CAD assembly was created from the conceptual design. First, PD was performed to split the conceptual design into components that fit within the MAM build volume. Detailed connections were then defined for the joining regions. Next, the conceptual design of the raw TO result was interpreted into a detailed CAD model. Finally, the build orientation for each component was selected considering support structure requirements and thermal distortion.

5.1 Part decomposition

The DMP Flex 350 MAM machine has a build volume of $275 \times 420 \times 275$ mm , however only $260 \times 360 \times 260$ mm of this volume is useable to account for the build plate height and any additional support structures. Part decomposition is needed because the dimensions of the conceptual design, at $602 \times 435 \times 35$ mm, were much larger than the MAM build volume shown in Figure 11.

The thickness of the conceptual design in the z-direction was extremely small compared to the x-and-y directions, so conceptual design can be simplified as two-dimensional for the purposes of PD. This made the PD process much simpler because the partitioning blocks only needed to rotate on the x-y plane rather than in 3D space. Therefore, three 2D partitioning blocks were defined with the same z-direction thickness as the conceptual design as shown in Figure 12.

As shown in Figure 13, the number of parts and joining regions depend on the type and orientation of the partitioning blocks. Using only the horizontal partitioning blocks in Figure 13 (a) required the largest number of parts and joining regions—four and six, respectively. The vertical and diagonal partitioning blocks have larger dimensions, reducing the number of parts and joining regions to three and four, respectively. The vertical and diagonal partitioning blocks resulted in a nearly identical division into parts and joining regions. The division into components also impacts important AM design criteria such as support material, support structure accessibility, and thermal behavior during printing. However, for this study, minimizing the number of the parts and joining regions was the primary design goal, and the divisions outlined in Figure 13 (b) and (c) were therefore selected.

It should be noted that the selection of partitioning blocks does not necessarily specify the exact printing orientation, as there are at least four possible orientations of each part within the partitioning block. The exact printing orientation for each part was selected in Section 5.4

5.2 Bolted joint design

As discussed in Section 3, bolted joints were selected because of their simplicity, lower risk, ease of disassembly,

Figure 10 Conceptual design of seat leg structure with an iso-filter applied using an element density threshold of 0.2 and simple averaging method: (a) side view, (b) isometric view
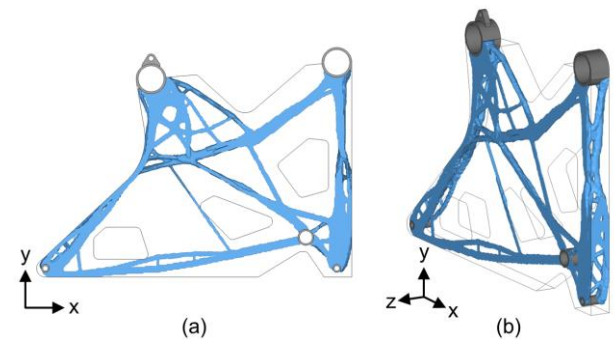

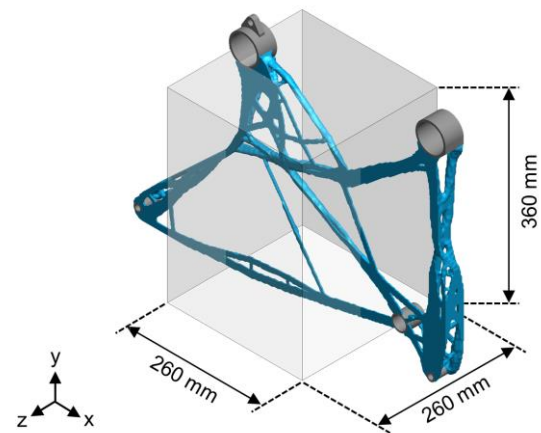**Figure 11** MAM build volume and conceptual design

Figure 12 Partitioning blocks with 35 mm thickness in the MAM build volume: (a) horizontal, (b) vertical, (c) diagonal
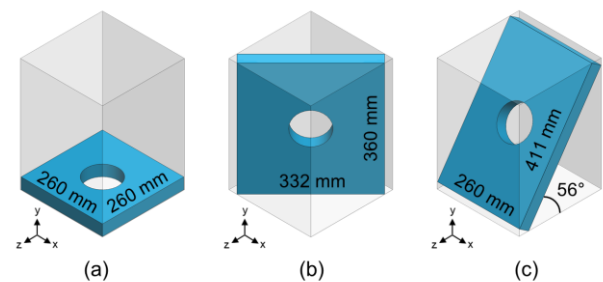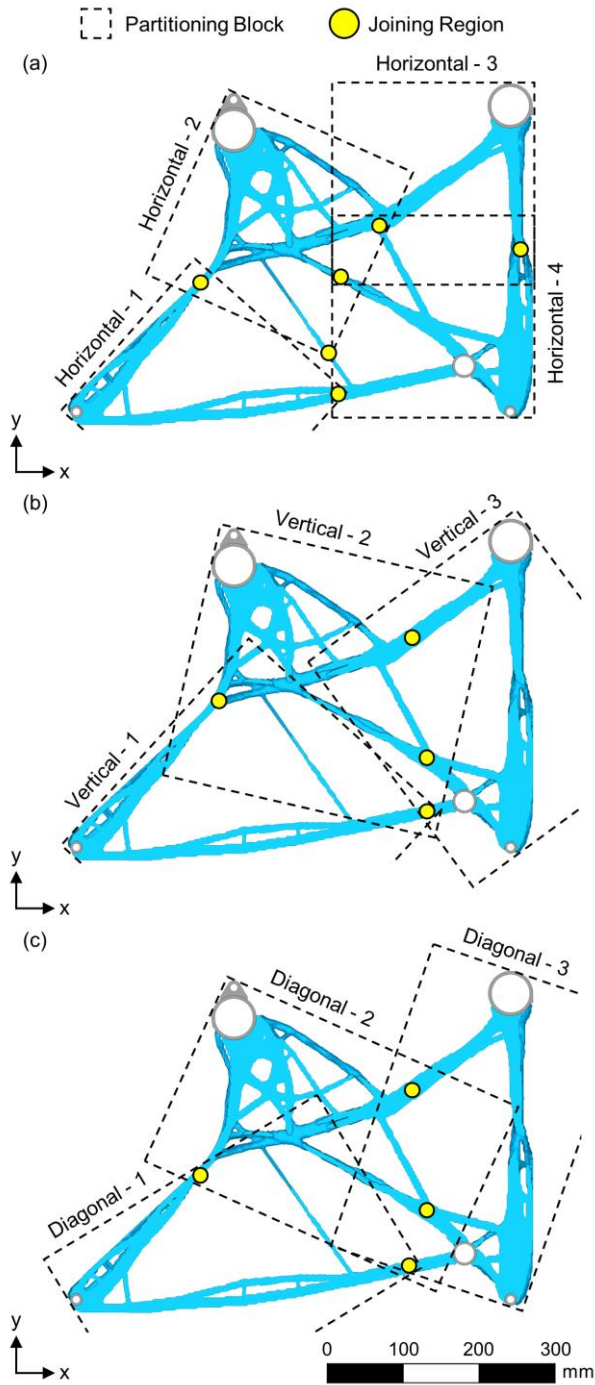
Figure 13 Options for part decomposition based on different partitioning blocks: (a) horizontal, (b) vertical, (c) diagonal

Figure 14 Bolted joint designs: (a) double bolted double lap joint, (b) double bolted single lap joint
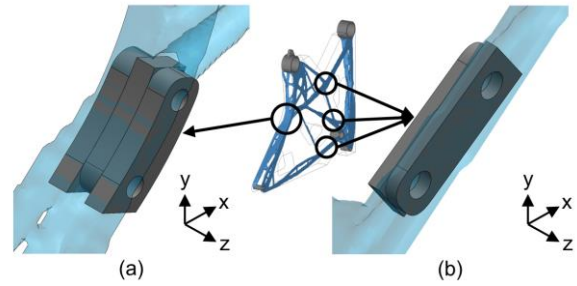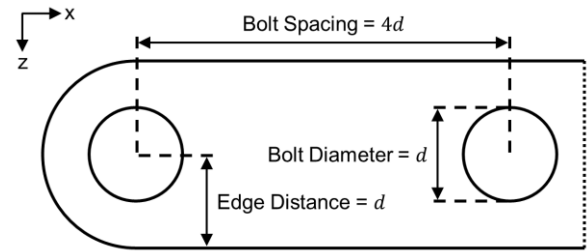

Figure 15 Dimensions of the bolted joint design

At this stage in the design process, it was assumed that an 8 mm bolt diameter d was sufficient for the double bolted design. In the Verification Phase, this bolt diameter could be updated based on the stress analysis results. Since there were no guidelines for bolted joint designs produced by titanium MAM, this study referred to general guidelines (Niu, 2001). Based on the limited design space of the partitioning blocks and the general guidelines, the minimum distance from the center of hole to edge was set to d, and the minimum distance between the centers of holes was set to $4d$ as shown in Figure 15.

5.3   CAD Modelling

Detailed CAD modelling was completed using SolidWorks version 2022, based on the conceptual TO result and the partitioning blocks shown in Figure 16. For the left component in Figure 16 (a), the location of the member indicated by the blue circle was adjusted to reduce the number of joining regions. For the middle component, the members in the red circle were simplified to the uniform and repetitive features as shown in Figure 16 (b). For the right component, the members in the magenta circle were combined to a single member to accommodate the bolted joint between the middle and right parts as shown in Figure 16 (c). The bolted joint connection between the left and right components was adjusted to fit into the overlapping region between the respective partitioning blocks as shown in the green circle in Figure 16 (a) and (c).

The preliminary CAD model of each part was assembled to form the seat leg structure shown in Figure

ease of maintenance, and reliable performance. Among bolted joints, lap and butt joints are often used to connect plates or members (Subramanian, 2011). Lap joints were selected for this project for their simple connection and lower material requirements compared to the butt joints. A double lap joint was used to connect the thicker region in Figure 14 (a), while single lap joints were used for the thinner joining regions shown in Figure 14 (b).

Figure 16 Preliminary CAD models of the decomposed seat leg structure: (a) left part, (b) middle part, (c) right part
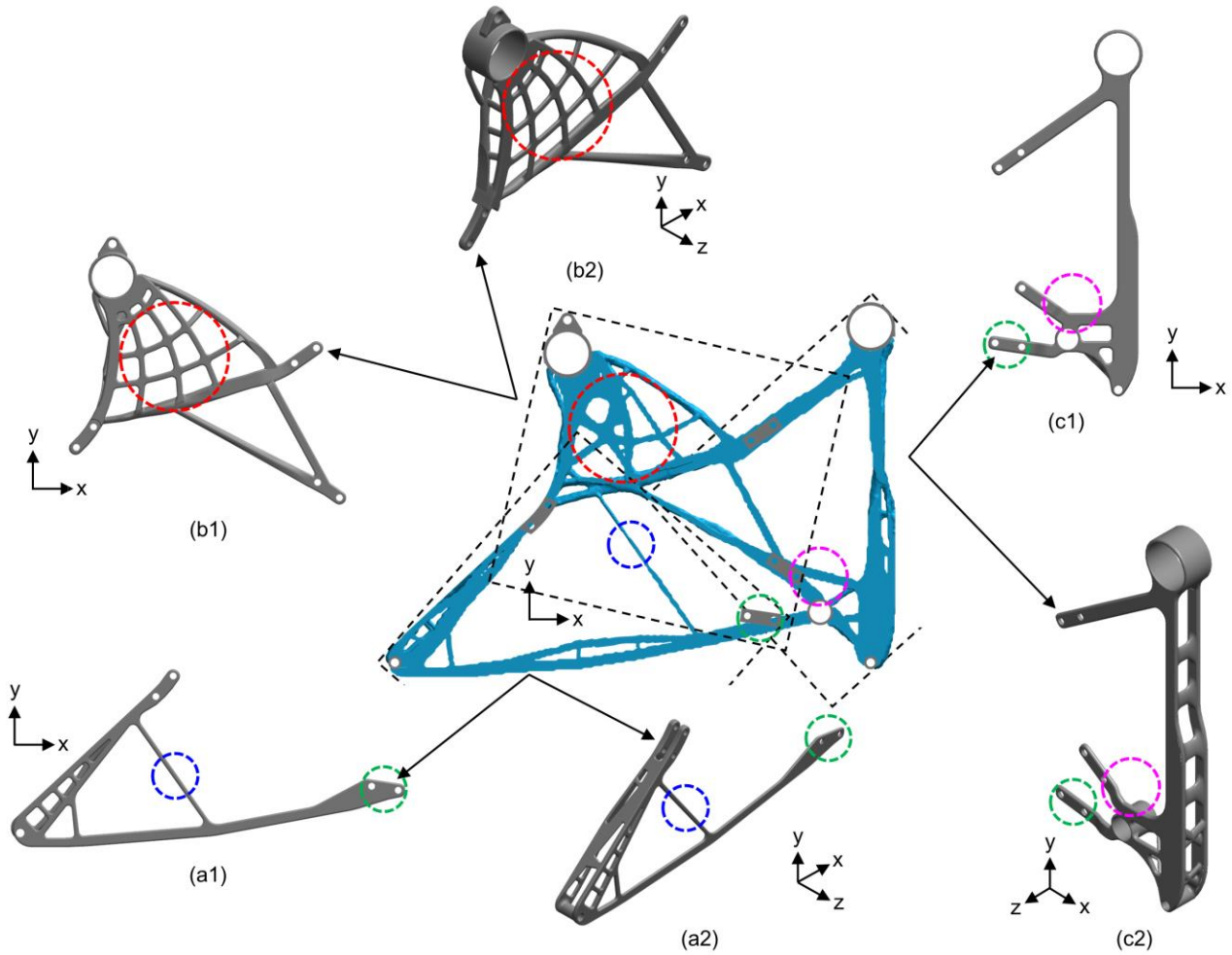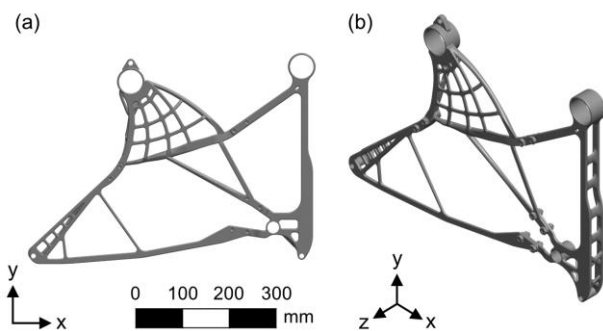

Figure 17 Preliminary design of the seat leg structure: (a) side view, (b) isometric view

17. At this stage, 8 mm bolts and nuts were added to the assembly, with 35 mm length for the double lap joint and 20 mm length for all other connections.

It is important to note that this detailed design was based on the conceptual TO results and did not consider the nonlinear behavior modelled in the crashworthiness analysis. Therefore, further design updates were needed in the Static and Dynamic Verification stage.

5.4 Build orientation selection

After CAD modelling, the build orientation of each part was selected. Note that the partitioning outlined in Figure 16 specified only the general position of each part within the portioning block, but not the build orientation on the component within the build volume. This study selected the vertical partitioning box from Figure 13 (b) rather than diagonal due to its more reliable printing behavior when considering thermal distortion. The diagonal print orientation can achieve reduced thermal distortion if the printing process parameters are optimized, but this was outside the scope of this study.

The vertical partitioning block had at least four possible build orientations, because the part can rotate within the rectangular shape of the partitioning block. In this study, support material, cross-sectional area, and tooling accessibility were used to select the build orientation for each part. These metrics were quantitatively and qualitatively summarized for each possible orientation in Table 4.

Support material is an important consideration because it directly influences material use, build time, and

Table 4 Comparison of support material, cross-sectional area, and tooling accessibility with four build orientation options for each part
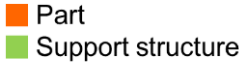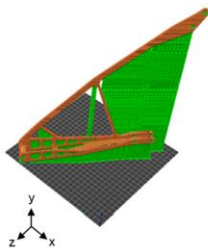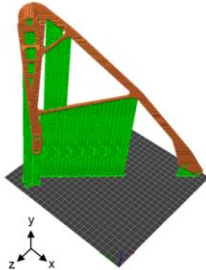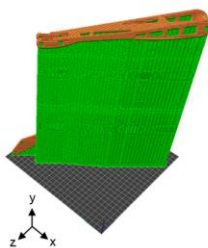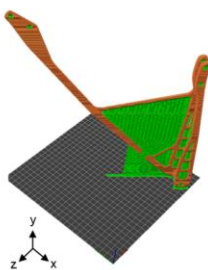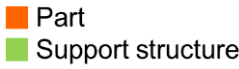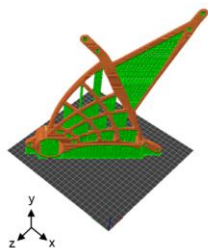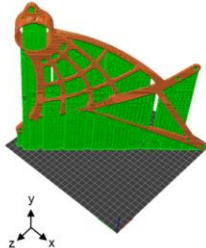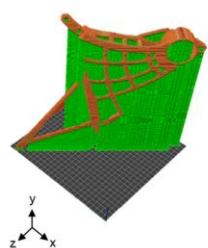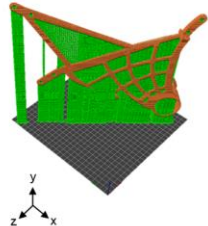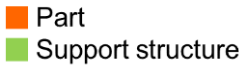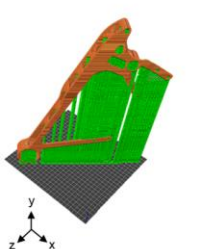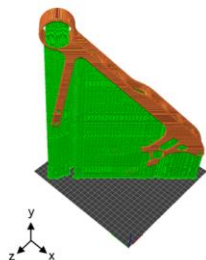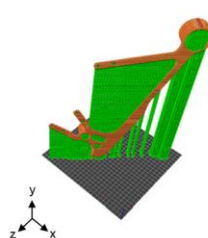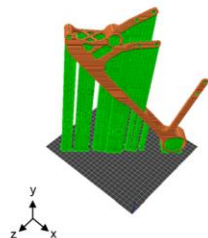
	Orientation A	Orientation B	Orientation C	Orientation D
Left Part				
Part / Support structure				
Relative Support Material	0.177	0.164	1.000	0.078
Cross-Sectional Area	Large	Small	Large	Small
Tooling Accessibility	Moderate	Moderate	poor	Moderate
Middle Part				
Part / Support structure				
Relative Support Material	0.231	0.591	1.000	0.421
Cross-Sectional Area	Moderate	Moderate	Moderate	Moderate
Tooling Accessibility	Good	Moderate	poor	Moderate
Right Part				
Part / Support structure				
Relative Support Material	0.780	1.000	0.630	0.700
Cross-Sectional Area	Large	Moderate	Large	Moderate
Tooling Accessibility	Moderate	poor	Moderate	Moderate

Figure 18 Example of poor tooling accessibility
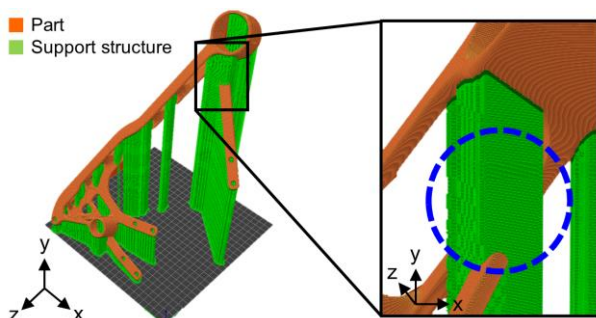
ultimately cost. Support material was quantitatively evaluated using PrusaSlicer version 2.6.1, which is a fused deposition modelling (FDM) slicer software that placed support material for any overhanging surfaces. At this stage, the addition of support structure to minimize part distortion or thermal stresses was not considered. Relative support material in Table 4 was calculated by normalizing results relative to the orientation with the highest support material. Thermal distortion and residual stresses can occur during the MAM printing process when there is large cross-sectional area in one printing layer or

when there is an abrupt change in cross-sectional area from one layer to the next. To avoid this, small cross-sectional areas and small incremental changes in cross-sectional areas are preferred. Table 4 includes a qualitative evaluation of cross-sectional area for each component. It is challenging and time consuming to remove support structures if they surround a structural member as shown in green in the blue dotted circle in Figure 18. In addition, support structures in enclosed or tight space within the part may be impossible to remove due to limited tooling accessibility. These aspects were qualitatively evaluated in Table 4 based on the support structures generated by the FDM slicer software.

Based on the assessment in Table 4, Orientation D was selected for the left part, because it had the lowest cross-sectional area and required the least amount of support material. For the middle part, all orientations had equivalent cross-sectional area, and therefore Orientation A was selected due to the decreased support structure and improved tooling accessibility. Orientation D was selected for the right part for its reasonable support material requirements and acceptable cross-sectional area and tooling accessibility compared to the other orientations.

6   Verification phase

In this section, static and dynamic verification was performed to ensure the seat leg design satisfied the structural requirements outlined in Section 2. The detailed design was updated in an iterative process shown in Figure 19 until the structural requirements were satisfied. The prototype of the seat leg structure was produced via the DMP Flex 350 MAM machine.

6.1   Static verification

Finite element modelling for static verification was performed using Altair HyperMesh version 2021.2 as shown in Figure 20 (a). The seat leg was meshed using approximately 650,000 tetrahedral elements of 2nd order with an element size ranging between 1 to 2 mm. The bolted joints were modelled using 1D rigid elements inside each bolted joint location, and a 1D rigid spring element between the 1D rigid elements as shown in Figure 20 (b) and (c). Rigid modelling saves computational cost compared to a high-fidelity bolt model without significantly altering the overall behavior of the model. The boundary conditions of the seat leg structure were defined to mimic the fixture of the aircraft seats as shown in Figure 21. The front legs were free to translate in x-direction and to rotate in y-direction. The rear legs were constrained in all translations and allowed to rotate in y- and-z directions.

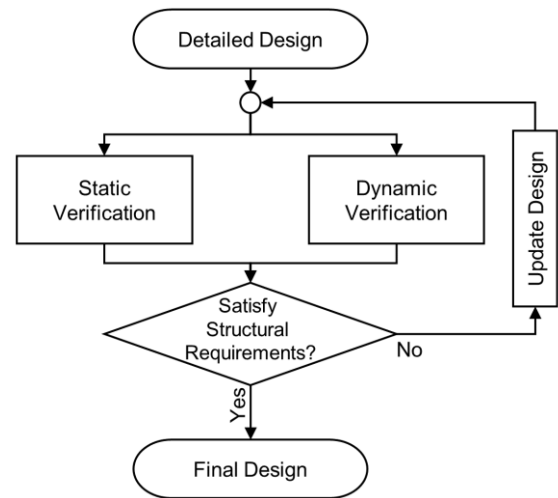**Figure 19** Iterative design update process to meet structural certification requirements

Figure 20 Finite element model for static verification: (a) aircraft seat leg, (b) bolted joint, (c) bolted joint modelling with transparent view
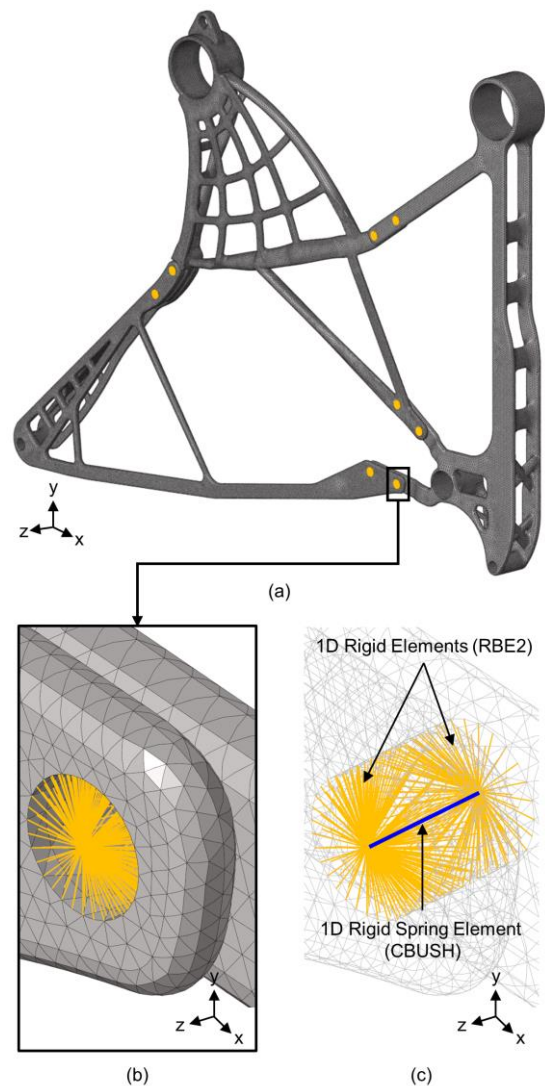
Figure 21 Boundary conditions for static verification
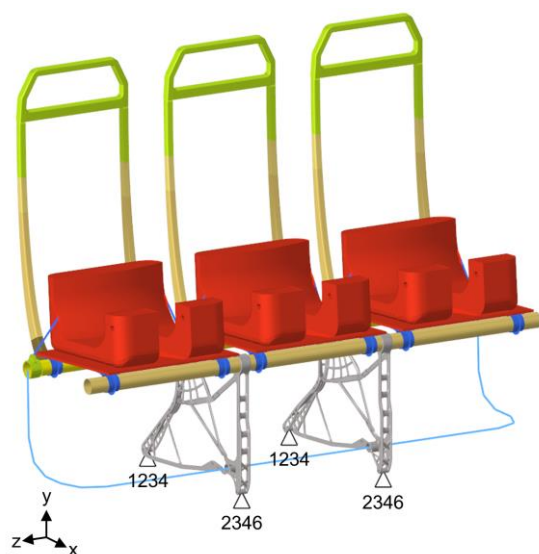
Table 5 Material properties of Ti-6Al-4V ELI (grade 23) after stress relief 2 (3D SYSTEMS, 2023)

Measurement	Horizontal	Vertical
Young's Modulus [GPa]	119 ± 3	120 ± 1
Yield Strength [MPa]	970 ± 30	1000 ± 60
Ultimate Strength [MPa]	1070 ± 30	1070 ± 30
Plastic elongation [%]	13 ± 2	13 ± 3
Density [g/cm^3]	4.42	

Figure 22 Linear static von Mises stress contour for LC 2.1: (a) bolted joint connecting left and middle parts, (b) rear tube at middle part of the right leg, (c) rear tube at middle part of the left leg, (d) bolted joint connecting middle and right parts
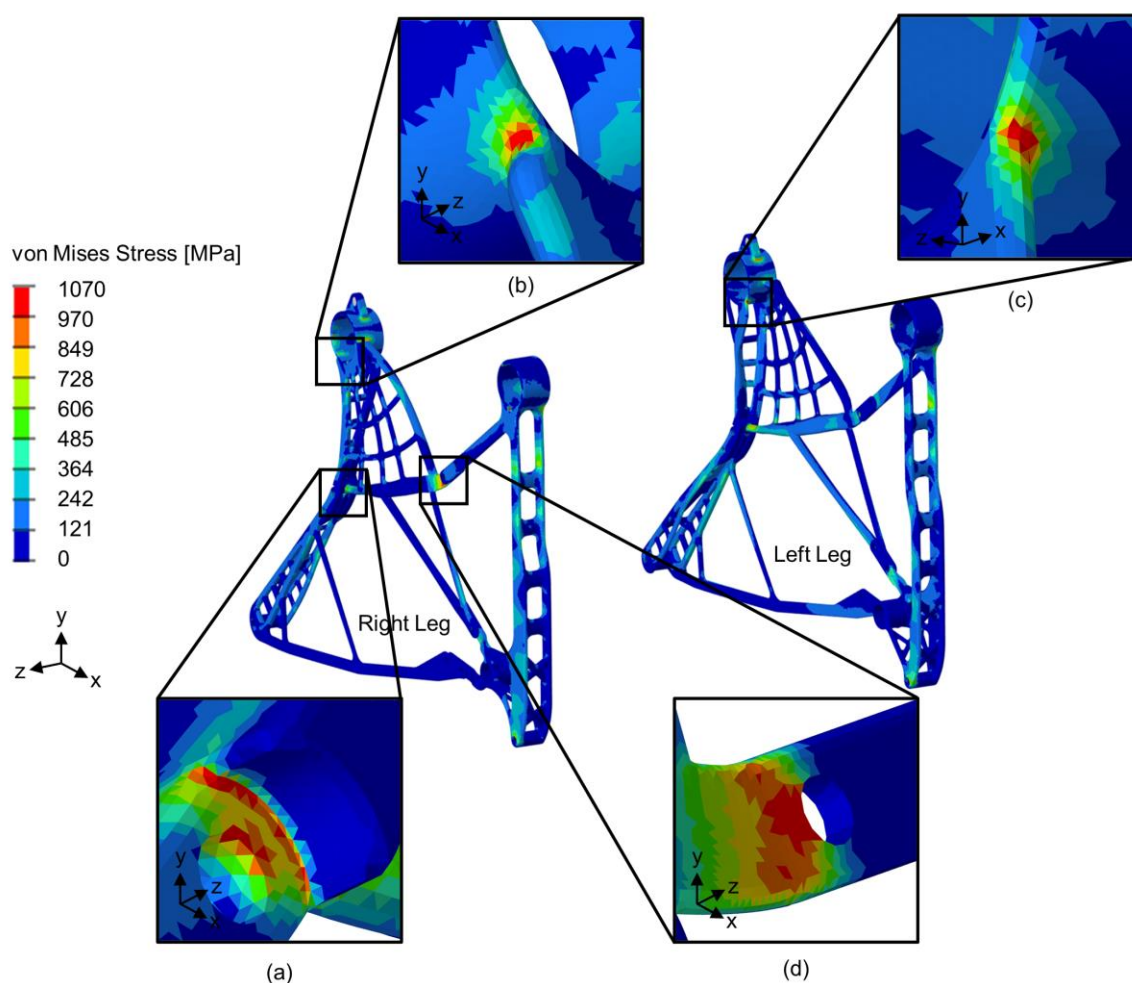
The static modelling used Ti-6Al-4V ELI (grade 23) material properties for the Metal AM components, which are summarized in Table 5 when produced with the DMP Flex 350 MAM machine (3D SYSTEMS, 2023). This study assumed the material properties were isotropic as there was little difference between the horizontal and

vertical directions. The average horizontal print direction properties were selected to provide a more conservative assumption. Poisson's ratio was not defined by the manufacturer, so this study used a generic value of 0.32 for titanium as defined in Section 4.

Linear static analysis was performed using Altair OptiStruct version 2021.2 as the FE analysis engine. To verify the seat leg structure complied with the static certification requirements, the minimum MoS described in Section 2.1 was calculated for all 13 static load cases. The preliminary results of the static verification are summarized in Table A2 of Appendix 2. For LC 2.1, stress concentrations exceeding the yield strength were observed as shown in Figure 22. The same high stress regions were observed in the opposite direction in LC 2.2. These stress concentrations occurred because of small fillet radii, which were increased in future design iterations. The high stress region shown in Figure 22 (d) was due to the abrupt changes in stiffness at the bolted connection and was addressed by increasing the member thickness.

Linear buckling analysis was conducted with the same software with results also summarized in Table A2. Buckling in the z-direction was observed at the red dotted circle in the left part in Figure 23. The same buckling region was observed in LC 1.3, 2.1, and 2.2. This buckling occurred because of the slender size of members connecting between the floor attachment points. This buckling was avoided by adjusting the width and thickness of the members in a future design change. Other than the failure points discussed above, which were rectified through minor design changes, the initial design passed the static certification requirements. These design changes are described in more detail in Section 6.3.

6.2   Dynamic verification

Dynamic verification simulates a crash scenario, where the seat structure may experience large displacement and

Figure 23 Buckling mode contour for LC 1.2

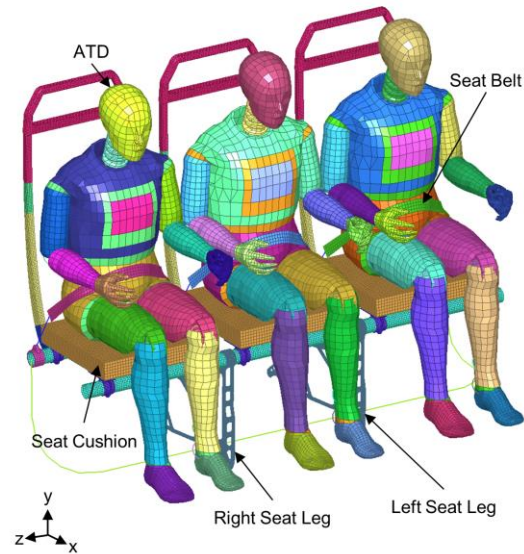**Figure 24** Finite element model for dynamic verification

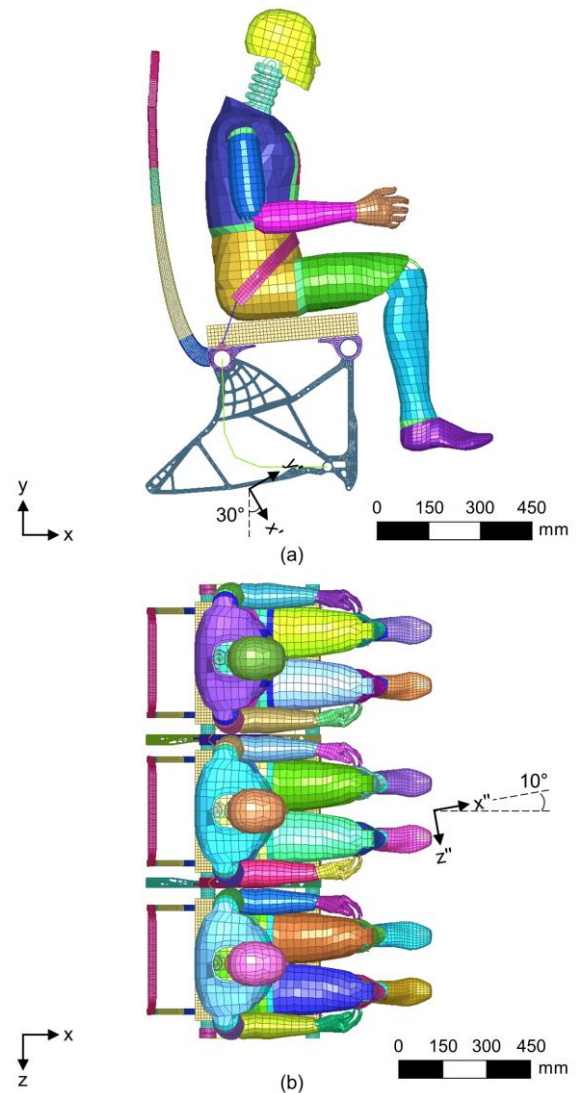**Figure 25** Global and local coordinate system: (a) dynamic test 1, (b) dynamic test 2
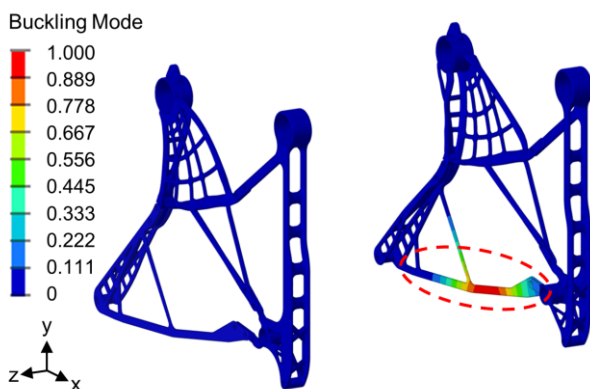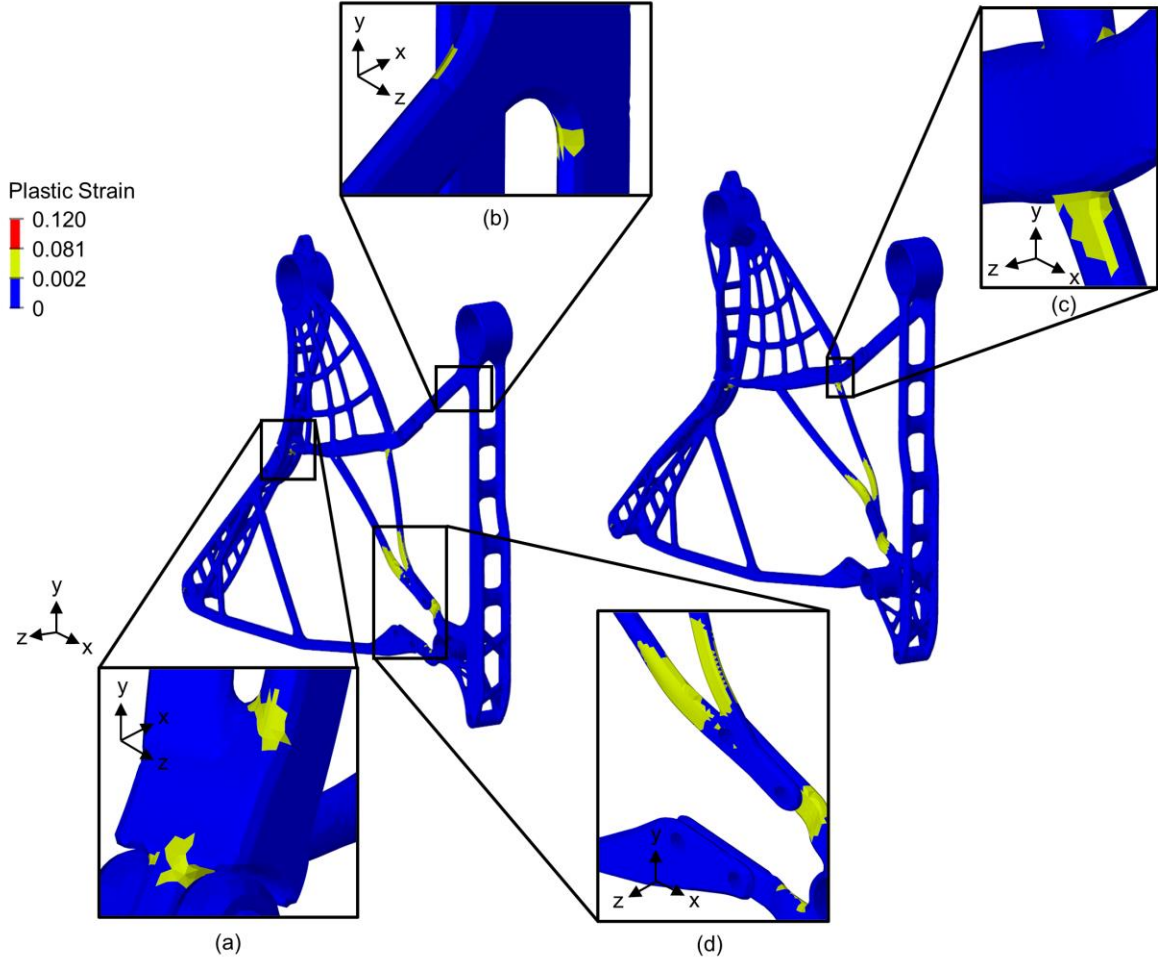
Figure 26 Plastic strain contour for the dynamic test 1: (a) left and middle parts of the right leg, (b) right part of the right leg, (c) middle part of the left leg, (d) middle and right parts of the right leg

material damage. The plasticity effects of the material must be considered to model large-displacement dynamic problems. The Johnson-Cook material model (Johnson and Cook, 1985) is commonly used in dynamic FE analysis, and was selected to capture the plasticity effects as follows:

$$\bar{\sigma} = \left(a + b\varepsilon_{plastic}^{n}\right)\left(1 + c\ln\frac{\dot{\varepsilon}}{\dot{\varepsilon}_0}\right)\left(1 - T^{*m}\right) \qquad (9)$$

where a is a yield stress, b is a strain modulus, c is a strain rate coefficient, $\varepsilon_{plastic}$ is a plastic strain, $\dot{\varepsilon}$ is a strain rate, $\dot{\varepsilon}_0$ is a reference strain rate, m is a temperature exponent, n is a hardening exponent, $\bar{\sigma}$ is a von Mises flow stress and T^* is a homologous temperature. This study did not account for the effects of strain-rate and temperature dependencies due to the limited knowledge of strain rate effects for MAM materials (Alkhatib and Sercombe, 2022). Therefore, only nonlinear stress-strain relationships were considered with the following values estimated from the properties in Table 5: $a = 900$ MPa,

$b = 585$ MPa $n = 0.328$, $c = 0$, $T^* = 0$, and failure plastic strain was 0.12.

Finite element modelling for dynamic verification was performed using Altair HyperMesh and HyperCrash version 2021.2, with the final model shown in Figure 24. The 50th percentile ATD, seat belt, and seat cushion were generated using HyperCrash. To reduce computational cost in dynamic analysis, the seat leg was re-meshed using approximately 245,000 tetrahedral elements of 2nd order with element size ranging between 1.5 and 3 mm. The total number of elements for the dynamic analysis model was approximately 644,000.

The loading conditions of dynamic test 1 and 2 described in Table 3 were used for the dynamic analysis model. For dynamic test 1, a local coordinate system was defined to restrict translation to the x'-direction as shown in Figure 25 (a). Other translations and all rotations were constrained at the floor fittings for both seat legs. An initial velocity of 10.67 m/s was applied to the entire model and the seat attachment points were decelerated according to the 14 G deceleration pulse. For dynamic test

Figure 27 Right seat leg fracture during floor deformation in the dynamic test 2
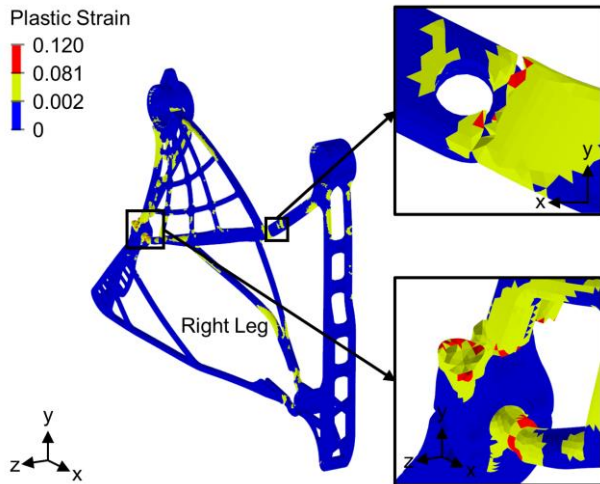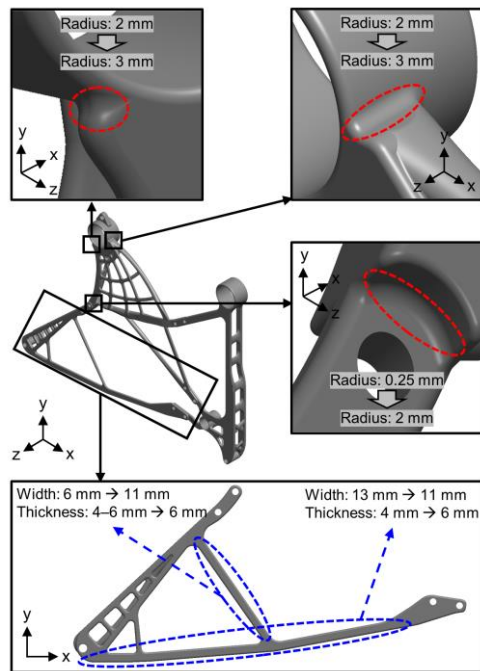

Figure 28 Design changes from static verification

2, floor deformation was applied to the floor fittings as per (SAE, 2020) prior to the deceleration pulse, resulting in a pre-stressing of the structure. Next, a local coordinate system was defined to restrict translation in x"-direction as shown in Figure 25 (b). Other translations and all rotations were constrained at the floor fittings for both seat legs. An initial velocity of 13.41 m/s was applied to the entire model and decelerated according to the 16 G deceleration pulse.

Dynamic analysis of the seat leg structure was performed using Altair Radioss version 2021.2 as the FE analysis engine. The minimum MoS described in Section

Figure 29 Several design changes from dynamic verification
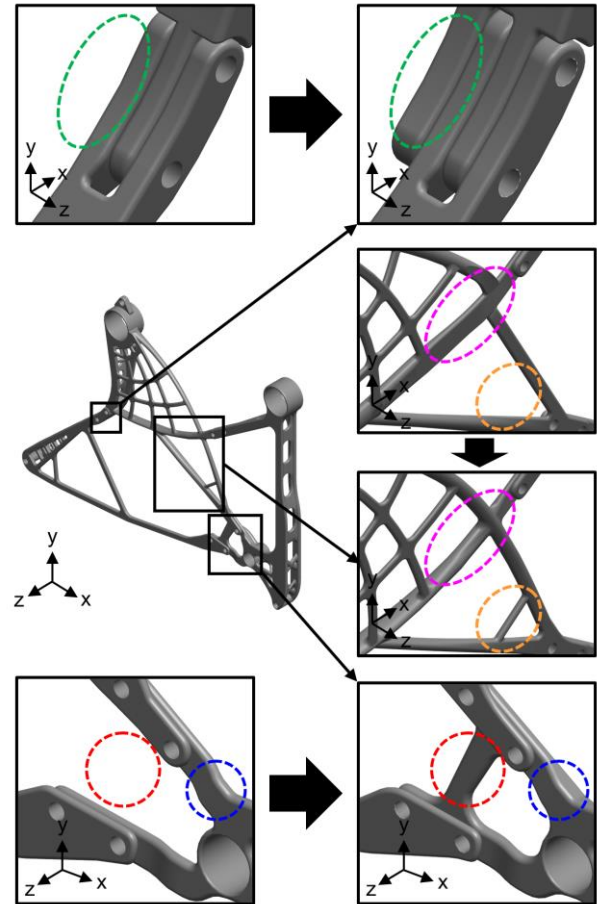
2.1 was calculated for each of the dynamic load cases. The preliminary results of dynamic test 1 are summarized in Table A3 of Appendix 2. High strain regions exceeding the elastic region were observed as shown in Figure 26. According to the dynamic certification requirements, yielding and small levels of damage are acceptable. This seat leg structure passed the dynamic test 1, with a minimum MoS values of 49%. However, fracture of several members was observed in dynamic test 2, as shown in Figure 27. Several iterations of design changes were needed to achieve a design that satisfied the dynamic test 2 criteria. These design changes are summarized in Section 6.3.

6.3 Final design

Design updates and subsequent analyses were iterated until the static and dynamic structural requirements were met. From the Static Verification, the fillet radii of several sharp corners were increased to reduce stress concentrations as shown in the red dotted circle in Figure 28. The width and thickness of the members marked with the blue dotted circle were adjusted to reduce buckling in z-direction. From the Dynamic Verification, additional design changes were performed as summarized in the

Figure 30 Final design of the seat leg structure: (a) side view, (b) isometric view
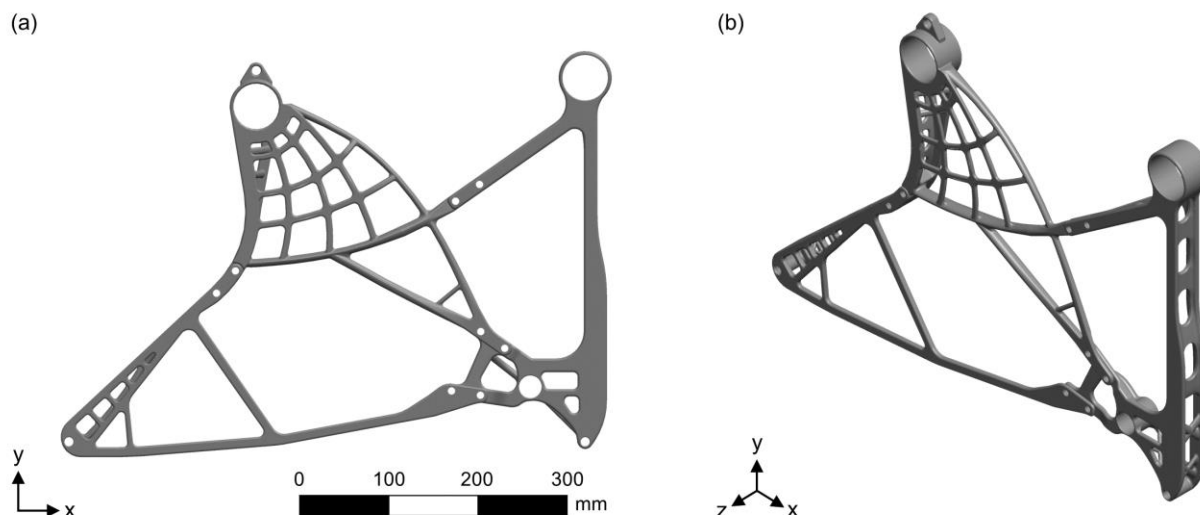

Table 6 Final results of static verification

Load Case	Seat Leg		Bolted Joint		
	MoS_{von} [%]	$MoS_{buckling}$ [%]	MoS_{axial} [%]	MoS_{shear} [%]	$MoS_{beraing}$ [%]
LC 1.1	166	458	1924	722	1416
LC 1.2	115	108	1789	440	1038
LC 1.3	115	108	1789	440	1038
LC 1.4	1089	553	20834	3696	6747
LC 1.5	494	2153	10367	1798	3323
LC 1.6	1497	4278	12045	4834	8994
LC 2.1	35	32	657	289	618
LC 2.2	35	34	656	290	619
LC 2.3	119	379	10982	408	817
LC 3.1	184	80	5869	2492	4677
LC 3.2	184	104	5869	2492	4677
LC 3.3	184	81	5876	2495	4683
LC 3.4	1159	107	27253	13845	21719

dotted circles in Figure 29. To prevent the fracture of the seat leg structure during the dynamic test 2 (in Figure 27), which occurred from severe buckling of the slender central members, the following updates were made: inclusion of additional members, modification of bolted joint regions, removal of cutouts at seat leg attachment points, and changing member cross-sections to increase thickness in z-direction. The final seat leg design that meets all certification requirements is pictured in Figure 30.

The final static verification results are summarized in Table 6. All MoS values are above zero, meaning the seat leg structure is safe from material fracture, geometric buckling, bolt fracture, and bearing failure for all 13 static load cases. It should be noted that LC 2.1 and LC 2.2 mimic 16 G dynamic load case, which is the most critical load case in structural airworthiness certification requirements, and the corresponding MoS values are therefore significantly lower than other static load cases.

The final dynamic verification results are summarized in Table 7. Dynamic test 1 resulted in a maximum plastic strain of 0.3%, which is significantly below the failure plastic strain. The seat leg structure can therefore be considered safe from fracture for dynamic test 1. For

Table 7 Final results of dynamic verification and several elemental plastic strain value from the highest

Load Case	Plastic Strain	$MoS_{plastic}$ [%]	Location
Dynamic Test 1	0.003	3900	Middle Part
	0.002	5900	Right Part
Dynamic Test 2	>0.120	-	Middle Part (5 elements) Left Part (8 elements)
	0.111	8	Left Part
	0.109	10	Left Part
	0.103	17	Middle Part
	0.094	28	Middle Part
	0.089	35	Right Part

Table 8 Comparative assessment between reference and final designs.

	Reference Design (Tzanakis *et al.,* 2023)	Final Design	Reduction [%]
Number of Parts	7	3	57
Number of Joining Regions	7	4	43
Mass of Seat Leg Structure	2.305	2.110	8.5

Figure 31 Plastic strain contour for the dynamic test 2: (a) floor deformation, (b) 16 G deceleration after floor deformation
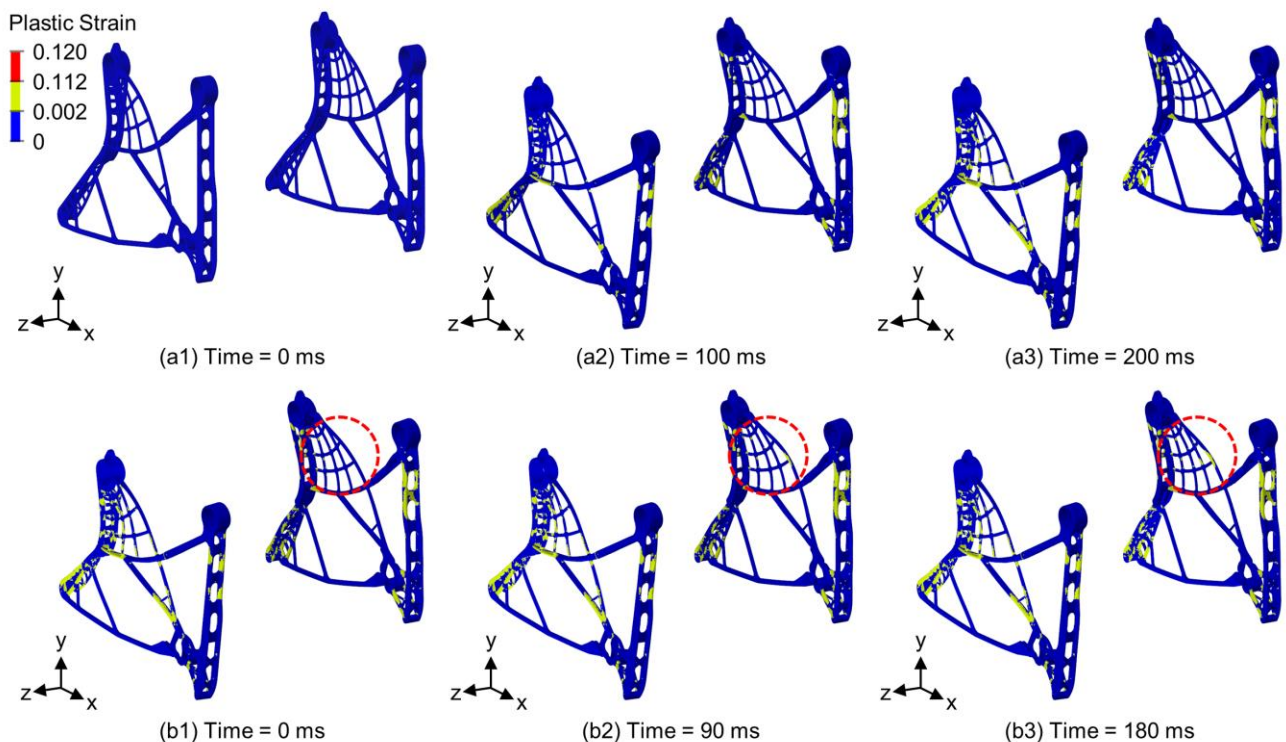
dynamic test 2, yielding was observed during the floor deformation in Figure 31 (a) and some buckling was observed during the 16G acceleration shown in the red dotted circle in Figure 31 (b). Thirteen elements exceeded the failure plastic strain and were deleted during the dynamic analysis, however, these elements failed in several isolated points distributed throughout the structure and did not represent the failure of a specific member of the component. The primary load paths of seat leg structure remained intact as shown in Figure 31 and this

Figure 32 Manufactured seat leg structure before support structure removal: (a) left part, (b) middle part, (c) right part
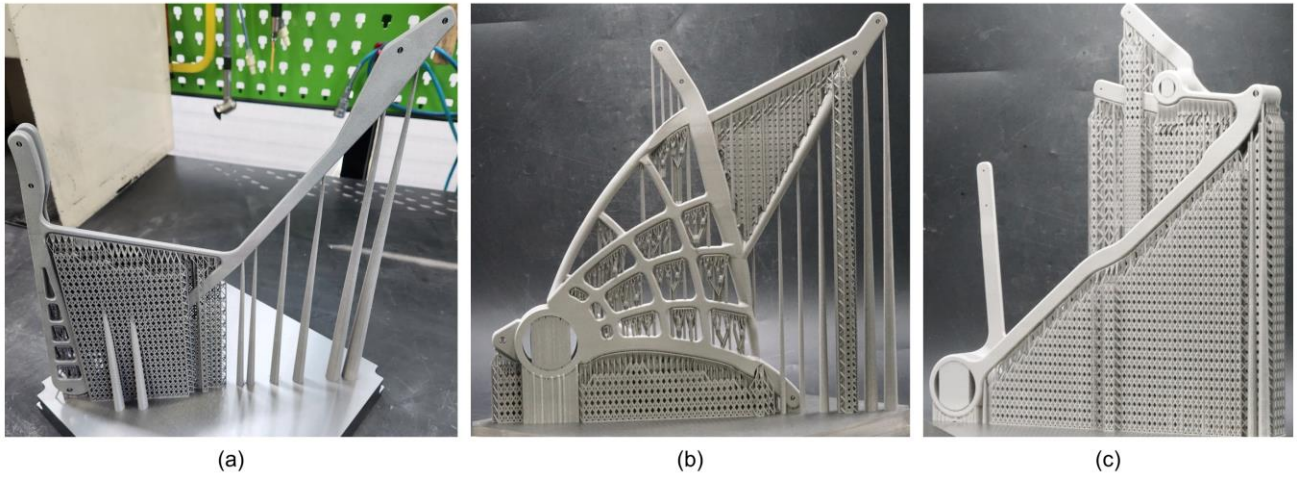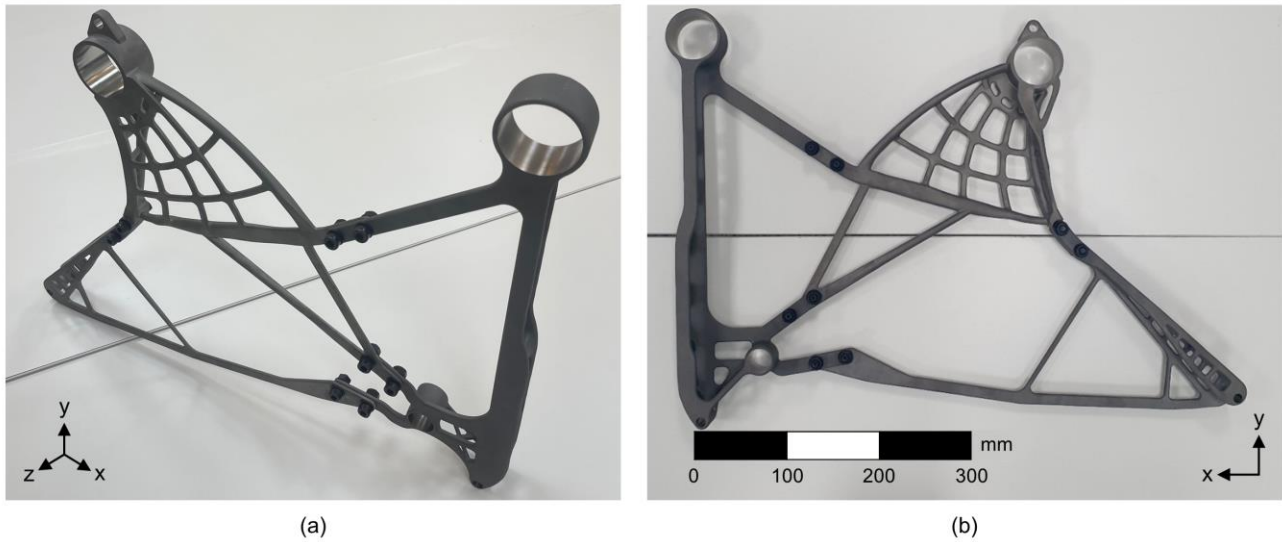

(a)   (b)   (c)

Figure 33 Manufactured seat leg structure assembly: (a) isometric view, (b) side view

(a)   (b)

load case is therefore deemed passed.

In summary, the final design of the seat leg structure satisfied the structural airworthiness certification requirements as all MoS values for static verification were above zero and the primary load paths remained intact during dynamic verification. Compared to the reference seat leg design (Tzanakis *et al.,* 2023), the final design achieved a significant reduction in the number of parts, the number of joining regions, and the mass of seat leg structure, as outlined in Table 8.

6.4   Prototype

The seat leg structure was produced via the DMP Flex 350 MAM machine with the following processes: 1) 3D printing, 2) heat treatment, 3) wire cutting, 4) machining of bolted holes, and 5) support removal. Support structures were added via 3DXpert software from 3D SYSTEMS. The manufactured seat leg structure is shown

in Figure 32 before removal of the support structure. After the post-processing, the manufactured seat leg structure was assembled as shown in Figure 33 (a). The parts were assembled using 8 mm diameter bolts and nuts. The size of the assembly is shown in Figure 33 (b).

7   Conclusions

This study designed a metal additive manufactured aircraft seat leg structure with reduced weight and part count relative to a reference design, while meeting certification requirements. This was accomplished through a new topology optimization design workflow specifically for additive manufacturing components larger than the build volume. In the Conceptual Design Phase, TO studies determined conceptual designs of the seat leg structure. In the Detailed Design Phase, the conceptual design was decomposed into three parts using the

partitioning blocks defined from the MAM build volume, which simplified the PD problem from 3D to 2D. The raw TO result for each part was interpreted into the detailed CAD assembly. The build orientation of each part was then selected based on a trade-off between support material requirements, cross-sectional area, and tooling accessibility. In the Verification Phase, static and dynamic verification was performed, and the design was updated to ensure the seat leg structure satisfied the structural requirements. Finally, the prototype of the seat leg structure was produced via the DMP Flex 350 MAM machine.

Overall, the conclusions of this work can be summarized as follows:

- The final seat leg design reduced mass by 8.5% and number of parts by 57% compared to the reference design (Tzanakis *et al.,* 2023)
- The seat leg structure was numerically verified to meet static and dynamic certification requirements and a physical prototype was fabricated using MAM
- The proposed workflow effectively partitioned a topology optimization result into an assembly that can be fabricated using metal additive manufacturing
- The partitioning blocks approach simplified part decomposition by reducing the dimensionality of the problem from 3D to 2D
- The 16G dynamic test with floor deformation was the most severe load case and influenced several design changes

While these results are promising, further improvements could be achieved in future studies. In the Conceptual Design Phase, including the floor deformation load case in the TO problem statement may have produced different load paths and reduced the number of changes necessary during the dynamic verification. Further studies could also investigate the impact of including dynamic loading on the topology optimization of an aircraft seat leg structure with the Equivalent Static Loading method. In the Detailed Design Phase, a computational PD optimization method is needed to determine the optimal location and rotation angle of partitioning blocks, particularly for complex 3D geometries. Lastly, a new build orientation optimization method that simultaneously considers support structure requirements and thermal distortion would further reduce costs and improve manufacturing reliability. An ideal topology optimization tool would simultaneously consider PD, joint design, support structure requirements, print orientation, and thermal deformation. However, significant advancements are needed in each of these research areas, and their integration into a holistic TO approach, before this tool could be applied to complex engineering design problems.

Conflict of interest

The authors declare that they have no conflict of interest.

References

Alkhatib, S.E. and Sercombe, T.B. (2022), "High strain-rate response of additively manufactured light metal alloys", *Materials & Design,* Vol. 217, doi: https://doi.org/10.1016/j.matdes.2022.110664.

Autodesk (2017), "Modern metal casting plus additive manufacturing equals paradise found(ry)" available at: https://www.autodesk.com/design-make/articles/metal-casting-and-additive-manufacturing (accessed 15 November 2023).

Bendsøe, M.P. and Kikuchi, N. (1988), "Generating optimal topologies in structural design using a homogenization method", *Computer Methods in Applied Mechanics and Engineering,* Vol. 71 No. 2, pp.197–224, doi: https://doi.org/10.1016/0045-7825(88)90086-2.

Bendsøe, M.P. and Sigmund, O. (2003), *Topology optimization: theory, methods, and applications,* Springer, Berlin, Heidelberg, Germany.

Berrocal, L., Fernández, R., González, S., Periñán, A., Tudela, S., Vilanova, J., Rubio, L., Martín Márquez, J.M., Guerrero, J. and Lasagni, F. (2019), "Topology optimization and additive manufacturing for aerospace components", *Progress in Additive Manufacturing,* Vol. 4, pp.83–95, doi: https://doi.org/10.1007/s40964-018-0061-3.

Blakey-Milner, B., Gradl, P., Snedden, G., Brooks, M., Pitot, J., Lopez, E., Leary, M., Berto, F. and Du Plessis, A. (2021), "Metal additive manufacturing in aerospace: A review", *Materials & Design,* Vol. 209, doi: https://doi.org/10.1016/j.matdes.2021.110008.

CFR (2023), "14 CFR part 25—Airworthiness standards: transport category airplanes", available at: https://www.govinfo.gov/app/details/CFR-2023-title14-vol1/CFR-2023-title14-vol1-part25 (accessed 13 November 2023).

Chan, C.K. and Tan, S.T. (2005), "Volume decomposition of CAD models for rapid prototyping technology", *Rapid Prototyping Journal,* Vol. 11 No. 4, pp.221–234, doi: https://doi.org/10.1108/13552540510612910.

Clausen, A. and Andreassen, E. (2017), "On filter boundary conditions in topology optimization", *Structural and Multidisciplinary Optimization,* Vol. 56, pp.1147–1155, doi: https://doi.org/10.1007/s00158-017-1709-1.

Fortune Business Insights (2022), "Aircraft seating market size, share & COVID-19 impact analysis", available at: https://www.fortunebusinessinsights.com/industry-reports/aircraft-seating-market-101680 (accessed 15 November 2023).

Fritz, K. and Kim, I.Y. (2020), "Simultaneous topology and build orientation optimization for minimization of additive manufacturing cost and time", *International Journal for Numerical Methods in Engineering,* Vol. 121 No. 15, pp.3442–3481, doi: https://doi.org/10.1002/nme.6366.

Guida, M., Manzoni, A., Zuppardi, A., Caputo, F., Marulo, F. and De Luca, A. (2018), "Development of a multibody system for crashworthiness certification of aircraft seat", *Multibody System Dynamics,* Vol. 44, pp.191–221, doi: https://doi.org/10.1007/s11044-018-9612-0.

Gulavani, O., Hughes, K. and Vignjevic, R. (2014), "Explicit dynamic formulation to demonstrate compliance against quasi-static aircraft seat certification loads (CS25. 561)–Part I: influence of time and mass scaling", *Proceedings of the Institution of Mechanical Engineers, Part G: Journal of Aerospace Engineering,* Vol. 228 No.11, pp.1982–1995, doi: https://doi.org/10.1177/095441001350633.

Holmberg, E., Torstenfelt, B. and Klarbring, A. (2013), "Stress constrained topology optimization", *Structural and Multidisciplinary Optimization,* Vol. 48, pp.33–47, doi: https://doi.org/10.1007/s00158-012-0880-7.

Hughes, K., Gulavani, O., Vuyst, T.D. and Vignjevic, R. (2014), "Explicit dynamic formulation to demonstrate compliance against quasi-static aircraft seat certification loads (CS25. 561)–Part II: Influence of body blocks", *Proceedings of the Institution of Mechanical Engineers, Part G: Journal of Aerospace Engineering,* Vol. 228 No.10, pp.1890–1903, doi: https://doi.org/10.1177/0954410013506415.

Ibhadode, O., Zhang, Z., Sixt, J., Nsiempba, K.M., Orakwe, J., Martinez-Marchese, A., Ero, O., Shahabad, S.I., Bonakdar, A. and Toyserkani, E. (2023), "Topology optimization for metal additive manufacturing: current trends, challenges, and future outlook", *Virtual and Physical Prototyping,* Vol. 18 No. 1, doi: https://doi.org/10.1080/17452759.2023.2181192.

Jang, H.H., Lee, H.A., Lee, J.Y. and Park, G.J. (2012), "Dynamic response topology optimization in the time domain using equivalent static loads", *AIAA Journal,* Vol. 50 No. 1, pp.226–234, doi: https://doi.org/10.2514/1.J051256.

Johnson, G.R. and Cook, W.H. (1985), "Fracture characteristics of three metals subjected to various strains, strain rates, temperatures and pressures", *Engineering fracture mechanics,* Vol. 21 No. 1, pp.31–48, doi: https://doi.org/10.1016/0013-7944(85)90052-9.

Kismarton, M.U. and Fullerton, J.A. (2013), "Composite seat pan structure for a lightweight aircraft seat assembly", *US Patent,* 8550564.

López-Castro, J.D., Marchal, A., González, L. and Botana, J. (2017), "Topological optimization and manufacturing by Direct Metal Laser Sintering of an aeronautical part in 15-5PH stainless steel", *Procedia Manufacturing,* Vol. 13, pp.818–824, doi: https://doi.org/10.1016/j.promfg.2017.09.121.

Morin, R. and Kim, I.Y. (2022) "Partitioning a topology-optimized structure into additively manufacturable parts using a feature-mapping approach: a novel decomposition optimization method", *Structural and Multidisciplinary Optimization,* Vol. 65 No. 10, p.298. doi: https://doi.org/10.1007/s00158-022-03394-8.

Niu, M.C.Y. (2001), *Airframe stress analysis and sizing,* Adaso/Adastra Engineering Center, Granada Hills, CA, USA.

Noronha, W., Joshi, V. and Jeyanthi, S. (2021), "Design of 3D printed aircraft seat structure using latticing in combination with topology optimization and generative design", *IOP Conference Series: Materials Science and Engineering,* Chennai, India, doi: https://doi.org/10.1088/1757-899X/1128/1/012008.

Oh, Y., Zhou, C. and Behdad, S. (2018), "Part decomposition and assembly-based (Re) design for additive manufacturing: A review", *Additive Manufacturing,* Vol. 22, pp.230–242, doi: https://doi.org/10.1016/j.addma.2018.04.018.

Oh, Y., Ko, H., Sprock, T., Bernstein, W.Z. and Kwon, S. (2021), "Part decomposition and evaluation based on standard design guidelines for additive manufacturability and assemblability", *Additive Manufacturing,* Vol. 37, doi: https://doi.org/10.1016/j.addma.2020.101702.

Olsen, J. and Kim, I.Y. (2020), "Design for additive manufacturing: 3D simultaneous topology and build orientation optimization", *Structural and Multidisciplinary Optimization,* Vol. 62, pp.1989–2009, doi: https://doi.org/10.1007/s00158-020-02590-8.

Prathyusha, A.L.R. and Babu, G.R. (2022), "3D printing Integration with Topology optimization for Innovative design and fabrication of Light Weight Aerospace Structures", *2022 International Conference on Recent Trends Microelectronics, Automation, Computing and Communications Systems (ICMACC),* Hyderabad, India, pp.547–552, doi: https://doi.org/10.1109/ICMACC54824.2022.1009338 6.

Roper, S.W.K., Lee, H., Huh, M. and Kim, I.Y. (2021), "Simultaneous isotropic and anisotropic multi-material topology optimization for conceptual-level design of aerospace components", *Structural and Multidisciplinary Optimization,* Vol. 64 No. 1, pp.441–456, doi: https://doi.org/10.1007/s00158-021-02893-4.

SAE (2015), "Analytical methods for aircraft seat design and evaluation", available at: https://doi.org/10.4271/ARP5765A (accessed 13 November 2023).

SAE (2018), "Aircraft seat design guidance and clarifications", available at https://doi.org/10.4271/ARP5526E (accessed 13 November 2023).

SAE (2020), "Performance standard for seats in civil rotorcraft transport aircraft, and general aviation aircraft", available at https://doi.org/10.4271/AS8049D (accessed 13 November 2023).

Seabra, M., Azevedo, J., Araújo, A., Reis, L., Pinto, E., Alves, N., Santos, R. and Mortágua, J.P. (2016), "Selective laser melting (SLM) and topology optimization for lighter aerospace componentes", *Procedia Structural Integrity,* Vol. 1, pp.289–296, doi: https://doi.org/10.1016/j.prostr.2016.02.039.

Shi, G., Guan, C., Quan, D., Wu, D., Tang, L. and Gao, T. (2020), "An aerospace bracket designed by thermo-elastic topology optimization and manufactured by additive manufacturing", *Chinese Journal of Aeronautics,* Vol. 33 No. 4, pp.1252–1259, doi: https://doi.org/10.1016/j.cja.2019.09.006.

Sigmund, O. (2007), "Morphology-based black and white filters for topology optimization", *Structural and Multidisciplinary Optimization,* Vol 33, pp.401–424, doi: https://doi.org/10.1007/s00158-006-0087-x.

Stachel, A., Steinmeyer, K. and Jussli, Z. (2020), "Aircraft seat device including force transferring carrier element", *US Patent,* 10814986.

Subramanian, N. (2011), *Steel structures: design and practice,* Oxford University Press, New Delhi, India.

Trivers, N.C., Carrick, C.A. and Kim, I.Y. (2020), "Design optimization of a business aircraft seat considering static and dynamic certification loading and manufacturability", *Structural and Multidisciplinary Optimization,* Vol. 62, pp.3457-3476, doi: https://doi.org/10.1007/s00158-020-02650-z.

Tzanakis, G., Kotzakolios, A., Giannaros, E. and Kostopoulos, V. (2023), "Structural analysis of a composite passenger seat for the case of an aircraft emergency landing", *Applied Mechanics,* Vol. 4 No. 1, pp.1–19, doi: https://doi.org/10.3390/applmech4010001.

Wiberg, A., Persson, J. and Ölvander, J. (2021), "An optimisation framework for designs for additive manufacturing combining design, manufacturing and post-processing", *Rapid Prototyping Journal,* Vol. 27 No. 11, pp.90–105, doi: https://doi.org/10.1108/RPJ-02-2021-0041.

Willner, R., Lender, S., Ihl, A., Wilsnack, C., Gruber, S., Brandão, A., Pambaguian, L., Riede, M., López, E., Brueckner, F. and Leyens, C. (2020), "Potential and challenges of additive manufacturing for topology optimized spacecraft structures", *Journal of Laser Applications,* Vol. 32 No.3, doi: https://doi.org/10.2351/7.0000111.

Zhou, Y., Nomura, T. and Saitou, K. (2019), "Multicomponent topology optimization for additive manufacturing with build volume and cavity free constraints", *Journal of Computing and Information Science in Engineering,* Vol. 19 No. 2, doi: https://doi.org/10.1115/1.4042640.

3D SYSTEMS (2023), "LaserForm Ti Gr23 (A)", available at: https://www.3dsystems.com/materials/laserform-ti-gr-23 (accessed 13 November 2023).

Appendix 1. Seat Structural Materials

Table A1 Material descriptions of aircraft seat components

Component	Material	Element Type
Baggage Bar	Al 2024-T351	BEAM
Forward and Rear Tubes	Al 2024-T351	SHELL
Seat Back	Long Fiber Prepreg Sheet (Roper et al., 2021)	SHELL
Seat Fitting	Al 2024-T351	SHELL
Seat Leg	Ti-6Al-4V ELI (grade 23)	SOLID
Seat Pan	Long Fiber Prepreg Sheet (Roper et al., 2021)	SHELL

Appendix 2. Preliminary results

Table A2 Preliminary results of static verification

Load Case	Seat Leg		Bolted Joint		
	MoS_{von} [%]	$MoS_{buckling}$ [%]	MoS_{axial} [%]	MoS_{shear} [%]	$MoS_{beraing}$ [%]
LC 1.1	52	125	17028	613	1044
LC 1.2	26	-16	8840	574	980
LC 1.3	26	-16	8840	574	980
LC 1.4	723	161	139469	3364	5455
LC 1.5	312	418	69686	1632	2677
LC 1.6	815	1302	102669	4179	6761
LC 2.1	-42	-47	4960	238	442
LC 2.2	-42	-46	4971	240	445
LC 2.3	24	51	10602	384	676
LC 3.1	88	79	44312	1424	2344
LC 3.2	88	103	44312	1424	2344
LC 3.3	89	80	44380	1428	2350
LC 3.4	763	107	156240	5979	9647

Table A3 Preliminary results of dynamic test 1 and several elemental plastic strain value from the highest

Plastic Strain	$MoS_{plastic}$ [%]	Location
0.081	48	Right Part
0.052	131	Middle Part
0.023	422	Middle Part
0.022	445	Middle Part
0.022	445	Right Part